Journal of Nonlinear Science (2025) 35:5
https://doi.org/10.1007/s00332-024-10096-6

Journal of Nonlinear Science

Pattern formation on regular polygons and circles

Thomas E. Woolley[1]

Received: 8 October 2024 / Accepted: 11 October 2024

Abstract
We investigate the formation of Turing patterns on regular polygonal domains, as the number of edges grow, leading to the limiting case of the circle. Using linear and weakly nonlinear analysis, and evidence by simulations, we demonstrate how the domain shape can fundamentally change the expected bifurcation structure. Specifically, on the square domain we are able to derive pitchfork bifurcations for stripe and spot solutions, as well as show that both branches cannot bifurcate to produce stable patterns. This compares with the case of the equilateral triangle domain that causes the Turing bifurcation to be generically transcritical and, in some cases, none of the bifurcating branches are stable. Moreover, we find a monotonically increasing, but nonlinear relationship, between the minimal bifurcation area and the number of edges. Thus, patterns can occur on triangles with much smaller areas than circles. Overall, this work raises questions for researchers who are simulating applications on domains with simple shapes. Specifically, even small changes to domain geometry can have large impacts on the produced patterns; thus, domain perturbations should be considered in any sensitivity analyses.

Keywords Turing pattern · Nonlinear analysis · Polygonal domain

Mathematics Subject Classification 35B36

1 Introduction

The formation of spatio-temporal complexity from simple rules is a research field with a long history (Maini et al. 1997, 2012; Krause et al. 2021; Woolley et al. 2017a). One of the most successful theories stems from one of Alan Turing's last works 'On the chemical basis of morphogenesis' published over 70 years ago (Turing 1952). The basic premise is to use the random motion of modelled agents as a destabilising

Communicated by Anthony Bloch.

✉ Thomas E. Woolley
woolleyt1@cardiff.ac.uk

[1] Cardiff School of Mathematics Cardiff University, Senghennydd Road, Cardiff CF24 4AG, UK

Published online: 03 November 2024

mechanism to generate patterns in the agent's population that would otherwise produce stable spatially homogeneous concentrations. In short, Turing patterns appear due to a diffusion-driven instability.

The resulting theory has been widely extended to include new phenomena, such as stochastic interactions, spatio-temporal heterogeneity, and domain growth (Schumacher et al. 2013; Cho et al. 2011; Maini et al. 2012; Woolley et al. 2017b; Aragón et al. 2012; Krause et al. 2020a; Crampin et al. 1999; Woolley et al. 2012). Equally, the theory has been applied successfully to many situations in biology and chemistry (Economou et al. 2012; Kondo and Asai 1996; Sheth et al. 2012; De Kepper et al. 1991; Ouyang and Swinney 1991; Fuseya et al. 2021; Tan et al. 2018; Rudovics et al. 1996; Ho et al. 2019; Hans et al. 2021) providing predictive power as to the outcome of new experiments and an understanding of the limitations of experimental systems.

With any theory with such a legacy, we must often revisit its roots to ensure that no generalisations have been missed, or to investigate whether new generalisations are possible due to work in other fields (Woolley et al. 2011a, b; Woolley 2011; Woolley et al. 2011c, 2021; Diego et al. 2018; Landge et al. 2020; Vittadello et al. 2021; Scholes et al. 2019). In this vein, we are going to consider a Turing unstable reaction–diffusion system on domains that are regular polygons and circles. The reason is that there has been a lot recent work in understanding which regular geometries have instabilities that are analytically tractable, allowing us to understand links between domain geometry and patterns better than ever before (McCartin 2011).

Specifically, it has long been known that the square has a tractable Laplacian structure as any solution can be written as a Fourier series written in terms of a trigonometric basis (Tolstov 2012). However, it has been recently proven that the square, triangle and derived structures are the only regular polygonal shapes that have a complete set of eigenfunctions of trigonometric form (McCartin 2011; Práger 1998; Fokas and Kalimeris 2014; McCartin 2003, 2002; Pockels 1891; Lamé 1833; Pinsky 1985, 1980). Although regular polygons will be our main focus, we will also mention non-regular polygonal half spaces such as the isosceles right triangle (a square halved along its diagonal) and the hemiequilateral triangle (a halved equilateral triangle, with interior angles $(\pi/2, \pi/3, \pi/6)$), which also have tractable solutions in terms of trigonometric functions.

Moreover, even if we cannot analytically investigate regular polygons with more than four edges, we are still able to simulate them and extract their bifurcation structure. This lead us to the limiting shape of the circle, and although the solution to the Laplacian eigenvalue problem on a circle does not have a trigonometric form, we can still make analytic headway by using Bessel functions.

But what of irregular shapes? If we were to consider rectangles and ellipses, which have two degrees of freedom defining their size. We could then easily consider an arbitrarily thin shape (effectively one-dimensional), which would support a Turing bifurcation, but have negligible area. Since we will be using bifurcation area as a means of comparing the polygons, we want to be able to remove such arbitrariness from discussion. Thus, we only consider regular polygons, circles and the half spaces mentioned previously.

Our goal is to investigate how the number of edges of a regular polygon influences the Turing bifurcation. Namely, even if the parameters of the reaction–diffusion system

are chosen such that the diffusion is able to drive a homogeneous steady state to instability, we still need the domain to be big enough to allow the instability to occur (Murray 2003). Thus, through weakly nonlinear analysis and simulation, we aim to track the minimum bifurcation area of polygons with increasing number of edges.

The reason for this investigation is because, as we will see, the relationship between number of edges and bifurcation area is certainly not obvious. Moreover, the number of edges can fully change the expected bifurcation structures that appear. Thus, although much work is done on square and rectangular domains, this work highlights a need for us to question our intuition of how the domain influences the patterns we generate. Further, it emphasises the requirement for researchers applying Turing patterns to experimental pattern formation systems to not only fully justify their domain of choice but also perturb it in their sensitivity analyses because as this and previous work has shown, the boundaries conditions and shape influence pattern formation more that we perhaps might think (Woolley et al. 2014a; Sheth et al. 2012).

We begin in Sect. 2, where we carefully define how we generate the polygonal domains on which we are going to simulate our results and how these relate to the domains on which we are doing derive analytically results. This leads to Sect. 3 where we revisit the standard partial differential equation theory behind Turing patterns. In Sects. 4–6, we algebraically investigate the linear and weakly nonlinear dynamics of Turing systems on equilateral triangular domains, square domains and circles. These theoretical results are evidenced in Sect. 7 leading to observations about how the bifurcation diagram depends on the number of edges of a regular polygonal domain. Finally, in Sect. 8, we provide an overarching view of our results concerning Turing structures on polygonal domains with increasing number of edges; we draw out commonalities, but more importantly highlight features that are different across the domains, which lead to future questions regarding the exact nature of the relationship between minimal bifurcation area and number of edges.

2 Geometry

We are going to be primarily considering flat, two-dimensional, regular polygons. As a means of creation for simulation purposes and for ease of comparison, we are going to define the vertices of the polygons using the complex roots of unity. Specifically, the equation $z^n = 1$ over the complex field (where I is defined to be the complex unit) has n distinct roots of the form $\exp(2\pi\, jI/n)$, $j = 0, 1, \ldots, n-1$. Using Euler's formula

$$z = \exp(2\pi\, jI/n) = \cos\left(\frac{2\pi\, j}{n}\right) + I \sin\left(\frac{2\pi\, j}{n}\right) \tag{1}$$

, we can identify the real and complex components of the solutions with the coordinates of the Cartesian plane, $(x, y) = (\cos(2\pi\, j/n), \sin(2\pi\, j/n))$. The points are equally spaced around the unit circle, $|z| = |x + Iy| = 1$, and, thus, provide a simple means of defining the vertices of the regular n-gon, $n \geq 3$ (see Fig. 1a). More generally, we can scale the polygons to be in circles of radius R by multiplying z by R.

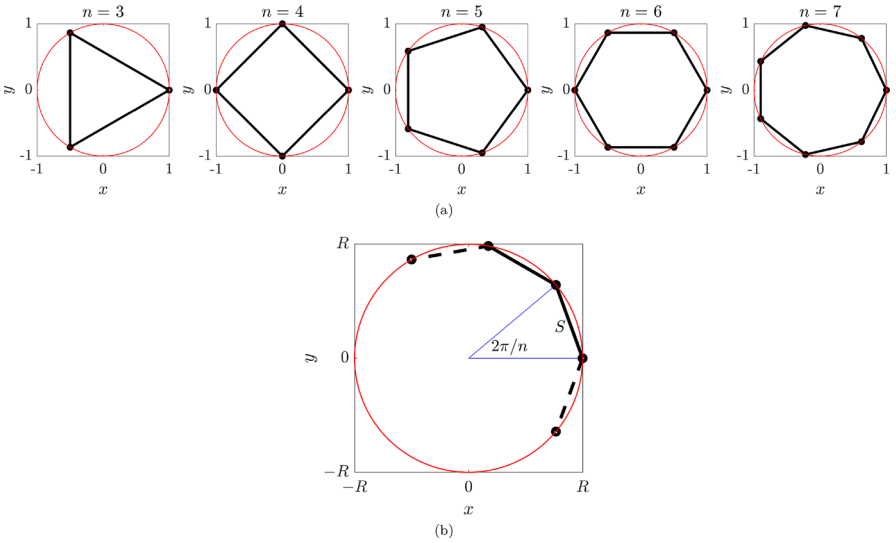

Fig. 1 **a** Examples of regular polygons, $n = 3, \ldots, 7$. The red circle illustrates the circle of unit radius. The roots of units of the black points highlighted on the circle and the polygon are then formed by connecting these points with black lines. **b** A schematic of one side of a general regular polygon with n sides. Using this figure and standard geometry, we are able to relate the radius size, R, the side length, S and the area, A of the polygon (Color figure online)

Critically, we are going to be considering R to be the bifurcation parameter of interest. Because, as is well known (Murray 2003) and will be highlighted in Sect. 4.2, it is not enough to ensure that the diffusion and kinetics are interacting in the correct way to ensure that a patterning instability can occur, we must also ensure that the space, on which the kinetics are acting, is large enough to support the intrinsic wavelength of the pattern. Thus, we will be looking for the minimum value of R (denoted R_c) at which the Turing instability can occur and a homogeneous steady state is driven unstable.

Consider now a general regular n-gon that has a circumcircle of radius R. A schematic of one side of the polygon is highlighted in Fig. 1b. The side length, S, and area A of the polygon are related to the radius through

$$S = 2R\sin(\pi/n), \tag{2}$$

$$A = nR^2\sin(2\pi/n)/2. \tag{3}$$

Note that as $n \to \infty$, then $S \to 0$ and $A \to \pi R^2$, which is to be expected because the polygon will begin to approximate a circle of radius R.

It should be noted that although using this definition provides a useful way of parametrising the domain for simulation purposes. Algebraically, it is easier to deal with rotated shapes. Namely, in future sections we will be considering Turing bifurcation analysis on the equilateral triangle, square and circle domains, as these shapes have tractable bifurcation structures. However, it is easier to derive these analytical

bifurcation results if one of the edges of the triangle and/or square is parallel to the horizontal axis. Since the two-dimensional Laplacian is invariant under rotation (as well as translation), such a rotation of the solution domain is immaterial.

3 Framework

Consider the following set of reaction–diffusion partial differential equations (PDEs)

$$\frac{\partial u}{\partial t} = D_u \nabla^2 u + f(u, v), \tag{4}$$

$$\frac{\partial v}{\partial t} = D_v \nabla^2 v + g(u, v), \tag{5}$$

which we are going to consider on the regular polygons as defined in Sect. 2. The parameters D_u and D_v are positive diffusion constants, $\boldsymbol{u} = (u, v)$ are the morphogen populations, and f and g describe the nonlinear interaction kinetics of u and v. To close the system, we need to provide boundary and initial conditions. These are now discussed at length.

We are going to be assuming that the PDE system presents a Turing instability. Thus, interaction equations f and g have at least one common root, *i.e.* (u_s, v_s), such that $f(u_s, v_s) = g(u_s, v_s) = 0$, that is stable in the absence of spatial dynamics, but can be driven unstable by the inclusion of diffusion. As such, we use the assumed steady-state existence to define the initial conditions for any domain. Namely, for each point in the spatial discretisation of a domain we sample a uniform random distribution with mean 0 and range $[-0.1, 0.1]$, add it to the steady state and take the absolute value (to ensure that the initial condition is nonnegative).

As for the boundary conditions, we are going to use zero-flux boundary conditions on all edges of the regular polygons. Few papers justify this choice and it is rarely questioned, as they are seen as fairly unconstrained boundary conditions (Woolley 2017; Ho et al. 2019; Adamer et al. 2020; Woolley et al. 2012; Winter et al. 2004; Schumacher et al. 2013; Weber et al. 2019). However, for our interests these conditions are critical as we want the Turing bifurcation on the square to be a supercritical pitchfork, which is the standard set up in most papers. Thus, any perturbation to the standard bifurcation structure will stem from the domain shape only.

Although boundary conditions do not influence the identification of the bifurcation point, R_c, through linear analysis they can fundamentally change the nonlinear bifurcation structure (Woolley 2022; Dillon et al. 1994). Specifically, on a square domain the Turing bifurcation is generically a pitchfork bifurcation under zero-flux boundary conditions (zero-Neumann boundary conditions) (Leppänen 2004; Benson et al. 1998; Crampin 2000; Dutt 2010, 2012; Grindrod 1996; Nicolis 1995; Auchmuty and Nicolis 1975; Bozzini et al. 2015; Breña-Medina and Champneys 2014; Dalwadi and Pearce 2022), but transcritical under extinction (zero-Dirichlet) boundary conditions, resulting in the possibility of patterns existing in the parameter region $R < R_c$ (Woolley 2022).

Further, we note that simply choosing zero-flux boundary conditions is not sufficient to ensure that subcritical patterns cannot exist in $R < R_c$. We must also choose kinetics that ensure the pitchfork bifurcation is supercritical, rather subcritical. Such kinetics are not rare and can easily be constructed based on the requirements of nonlinear analysis (Woolley et al. 2021; Bozzini et al. 2015). Critically, our derivations are independent of assumptions on the kinetics and the assumption of a supercritical bifurcation simply assures that the analytically derivable value of R_c is a minimum (at least on a square domain).

Although the theory is independent of a given set of kinetics, we will be using the Schnakenberg system for illustrative purposes (Gierer and Meinhardt 1972; Schnakenberg 1979). This not to say that the kinetics are particularly relevant to a given application, just that they are a well-studied set of Turing unstable reaction kinetics that provide the required supercritical pitchfork bifurcation on a square domain (Winter et al. 2004; Woolley et al. 2010; Adamer et al. 2020).

4 Linear analysis

4.1 Spatially homogeneous stability

The first condition of a Turing instability taking place is that there exists a steady state that is stable in the absence of diffusion. Since this removes the idea of space from the system, the derivation of the required conditions is the same over all domain shapes.

We consider a spatially independent perturbation around the steady state,

$$\begin{pmatrix} u \\ v \end{pmatrix} = \begin{pmatrix} u_s \\ v_s \end{pmatrix} + \begin{pmatrix} \epsilon_u \\ \epsilon_v \end{pmatrix} \exp(\lambda t), \tag{6}$$

where $0 < |\epsilon_u|, |\epsilon_v| \ll 1$. Substituting equation (6) into equations (4) and (5) and linearising the system, we generate the following eigenvalue problem,

$$\lambda \begin{pmatrix} \epsilon_u \\ \epsilon_v \end{pmatrix} = \begin{pmatrix} f_u & f_v \\ g_u & g_v \end{pmatrix} \begin{pmatrix} \epsilon_u \\ \epsilon_v \end{pmatrix} = \boldsymbol{J} \begin{pmatrix} \epsilon_u \\ \epsilon_v \end{pmatrix}, \tag{7}$$

where $\boldsymbol{J}$ is the Jacobian matrix. The λ that satisfy equation (7) satisfy the auxiliary equation,

$$\lambda^2 - \lambda(f_u + g_v) + f_u g_v - f_v g_u = 0. \tag{8}$$

From the Routh–Hurwitz condition, the roots of equation (8) have negative real part (and the steady state is, thus, stable) if and only if

$$Tr(\boldsymbol{J}) = f_u + g_v < 0, \tag{9}$$

$$Det(\boldsymbol{J}) = f_u g_v - f_v g_u > 0, \tag{10}$$

where Tr and Det are the trace and determinant functions acting on $\boldsymbol{J}$, respectively. Equations (9) and (10) are the necessary conditions for the spatially homogeneous state to be stable without diffusion.

4.2 Spatially heterogeneous stability

Extending our understanding of instability to include spatial perturbations will depend on converting the Laplacian operator into a linear functional. Namely, we want to solve

$$\nabla^2 h = -k^2 h \tag{11}$$

with appropriate boundary conditions on whatever domain shape we are interested in. Solving equation (11) numerically is fairly simple for modern computers (Shortley and Weller 1938) and has applications in understanding vibrational modes of a free elastic membrane, acoustic ducts with hard walls and in the propagation of electromagnetic waves (Jones 1986; Sabatini 2018).

There has also been much work done on analytically understanding the eigenvalues of the Laplace operator (McCartin 2011; Práger 1998; Fokas and Kalimeris 2014; McCartin 2003, 2002; Pockels 1891; Lamé 1833; Pinsky 1985, 1980) culminating in a characterisation of all polygonal shapes that have trigonometric eigenfunctions. Namely, the only polygonal domains that possess a complete set of trigonometric eigenfunctions that solve the Laplacian with either Dirichlet or Neumann boundary conditions are the rectangle, the square, the isosceles right triangle, the equilateral triangle and the hemiequilateral triangle (a halved equilateral triangle, with interior angles $(\pi/2, \pi/3, \pi/6)$) (McCartin 2011). Alongside these polygonal domains we will also be investigating circular domains, which will require us to make use of Bessel function, which can be generalised to Mathieu functions should we want to consider elliptical domains (Gutiérrez-Vega et al. 2003; Khosravian-Arab et al. 2017).

In the next few subsections, we will be going over the details for each domain, namely what the Laplacian form is, what the general eigenexpansion solution is and how this defines k. However, presently we can continue under the assumption that in each case we can solve the Laplacian equation in the form of equation (11). We use a perturbation of the form

$$\boldsymbol{u} = \begin{pmatrix} u \\ v \end{pmatrix} = \begin{pmatrix} u_s \\ v_s \end{pmatrix} + \begin{pmatrix} \epsilon_u \\ \epsilon_v \end{pmatrix} \exp(\lambda t) h(\boldsymbol{x}) \tag{12}$$

Linearising the equations and substituting in equation (11) provide

$$\lambda \begin{pmatrix} \epsilon_u \\ \epsilon_v \end{pmatrix} = -k^2 \begin{pmatrix} D_u & 0 \\ 0 & D_v \end{pmatrix} \begin{pmatrix} \epsilon_u \\ \epsilon_v \end{pmatrix} + \begin{pmatrix} f_u & f_v \\ g_u & g_v \end{pmatrix} \begin{pmatrix} \epsilon_u \\ \epsilon_v \end{pmatrix} = \left(-k^2 \boldsymbol{D} + \boldsymbol{J} \right) \begin{pmatrix} \epsilon_u \\ \epsilon_v \end{pmatrix}, \tag{13}$$

where $\boldsymbol{D}$ is an appropriately defined matrix of diffusion coefficients.

The accompanying auxiliary equation of the eigenvalue problem in equation (13) is

$$0 = \lambda^2 - Tr\left(\boldsymbol{J} - k^2 \boldsymbol{D} \right) \lambda + Det\left(\boldsymbol{J} - k^2 \boldsymbol{D} \right). \tag{14}$$

Since $Tr(\boldsymbol{J}) < 0$ is required, we can deduce that $Tr\left(\boldsymbol{J} - k^2 \boldsymbol{D} \right) < 0$. Thus, by applying the Routh–Hurwitz condition, once again, we see that the only way to drive the system to instability is to ensure that $Det\left(\boldsymbol{J} - k^2 \boldsymbol{D} \right) < 0$. Namely,

$$\left(f_u - k^2 D_u\right)\left(g_v - k^2 D_v\right) - g_u f_v < 0. \tag{15}$$

Inequality (15) can be seen as a quartic in k, or a quadratic in k^2. Thus, it is possible to satisfy inequality (15) whenever we can choose k^2 that satisfies

$$k_-^2 < k^2 < k_+^2, \tag{16}$$

where

$$k_\pm^2 = \frac{D_u g_v + D_v f_u \pm \sqrt{(D_u g_v + D_v f_u)^2 - 4 D_u D_v (f_u g_v - g_u f_v)}}{2 D_u D_v}, \tag{17}$$

Critically, we note that for $k_\pm^2$, to exist we require

$$(D_u g_v + D_v f_u) > 2\sqrt{D_u D_v (f_u g_v - g_u f_v)} > 0,$$

which is another necessary condition for Turing instabilities to take place. Further, we note that the values of $k_\pm$ are defined by the reaction and diffusion parameters. Thus, if these parameters are fixed, then $k_\pm$ is the same in all cases regardless of the polygonal domain on which the simulation is occurring.

The final necessary condition is to ensure that there exist viable k^2 that satisfy inequality (16). In the cases, where the domain size and k have a tractable relationship, we note that they are inversely proportional (McCartin 2011). Thus, since we are considering the domain size to be the bifurcation parameter, then increasing the domain size is equivalent to reducing k and the Turing bifurcation will happen when the first nonzero eigenvalue is equal to k_+, *i.e.* $k = k_+$.

Over the next few sections, we investigate the cases in which the values of k have either a closed-form expression or can be specified as the solution of an algebraic equation. Critically, we want to compare how these values differ across the domain geometries, as well as over the possible multiplicity of solutions available.

5 Deriving smallest homogeneous steady-state bifurcation points over regular two-dimensional domains

In this section, we are going to apply the theory derived in Sect. 4 to Turing systems on regular polygonal domains. Since we will be varying the number of edges of the polygonal domains (increasing them to their circular limit), it perhaps makes sense to start with a triangular domain and increase the number of edges from there. However, we initially start with a square domain due to the simple form the eigenfunctions and eigenvalues take, its repeated use in the literature and familiarity the reader may have for the derivation of the Turing bifurcation on such domains (Murray 2003; Maini and Woolley 2019; Maini et al. 2016; Woolley et al. 2017b, a; Woolley 2011; Aragón et al. 2012; Maini et al. 2012; Woolley 2022; Krause et al. 2020b; Woolley et al. 2014b; Krause et al. 2018, 2020a). Having considered the square domain, we then consider the equilateral triangle and circular domains afterwards.

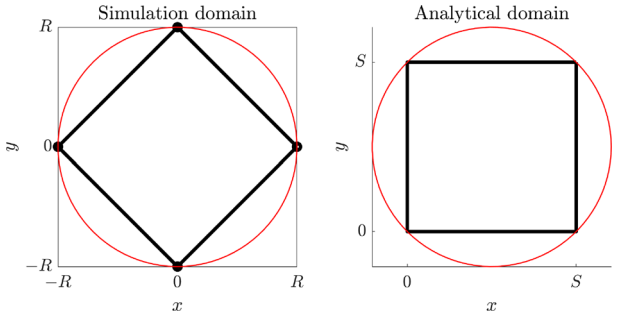

Fig. 2 Rotating and translating the polygon formed by the roots of unity provide the domain on which we will be algebraically deriving the Turing bifurcation point

5.1 Square domain

With respect to the geometry presented in Sect. 2, we are going to consider a square of side length S in a circumcircle of radius R, centred at the origin. The domain we are going to analytically work on when compared to the simulation solution domain is rotated by $\pi/4$ radians and then translated be the vector $(S/2, S/2)^T$ (see Fig. 2). Using Pythagoras' theorem, or equation (2), we can then relate $R = S/\sqrt{2}$.

The reason for this affine transformation is that the Laplacian and zero-flux boundary conditions have a particularly simple form on the domain $[0, S] \times [0, S]$. Specifically, the Laplacian in the standard Cartesian coordinates is

$$\nabla^2 = \frac{\partial^2}{\partial x^2} + \frac{\partial^2}{\partial y^2} \tag{18}$$

and the zero-flux boundary conditions for u are

$$\frac{\partial u}{\partial x}(0, y) = \frac{\partial u}{\partial x}(S, y) = \frac{\partial u}{\partial y}(x, 0) = \frac{\partial u}{\partial y}(x, S) = 0, \tag{19}$$

with the same boundary conditions for v, mutatis mutandis.

Furthermore, this redefinition of the geometry allows the general solution to have a particularly simple eigenexpansion solution

$$\begin{pmatrix} u \\ v \end{pmatrix} = \begin{pmatrix} u_s \\ v_s \end{pmatrix} + \sum_{m,n} \begin{pmatrix} c_{umn} \\ c_{vmn} \end{pmatrix} \cos(k_m x) \cos(k_n y), \tag{20}$$

where $k = \sqrt{k_m^2 + k_n^2}$ and $k_m = m\pi/S$ and $k_n = n\pi/S$ for $n, m \in \mathbb{N}$ and the coefficients (c_{umn}, c_{vmn}) are specified in a given application, but kept general here.

Ignoring the homogeneous solution, $k_0 = 0$, the first heterogeneous solution occurs when $k = \pi/S$, which happens when $(k_m, k_n) = (k_1, k_0) = (\pi/S, 0)$, $(k_0, k_1) = (0, \pi/S)$. Equating this with equation (17), we get that the first bifurcation happens when $\pi/S = k_+$. Thus, the bifurcation length of the square is $S_c = \pi/k_+$,

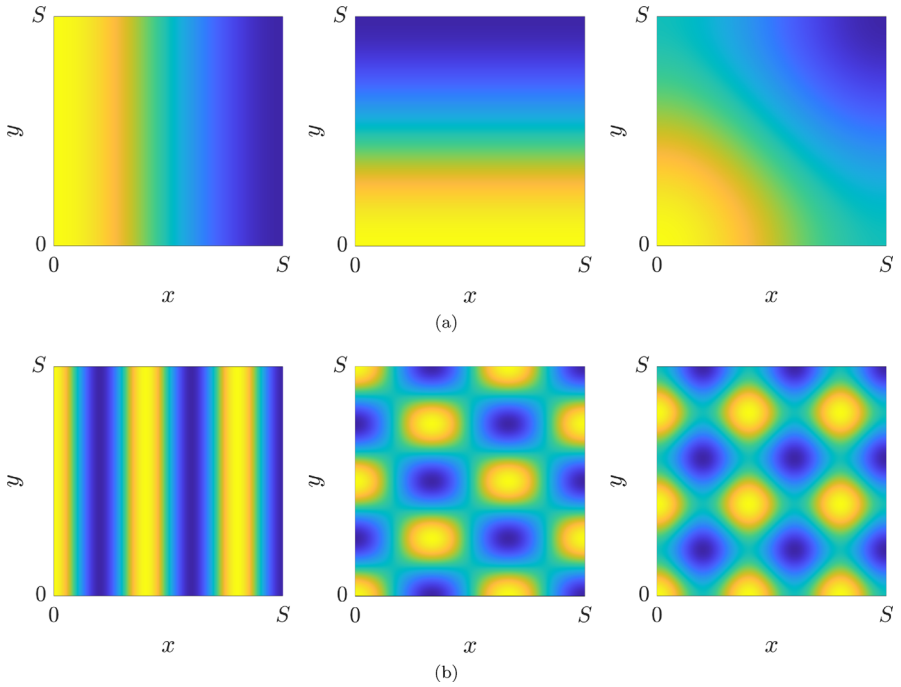

Fig. 3 Illustrating unstable modes and their possible symmetries. **a** From left to right, we have the first three possible unstable trigonometric modes: $\cos(\pi x/S)$, $\cos(\pi y/S)$ and $(\cos(\pi x/S) + \cos(\pi y/S))/2$. **b** From left to right, we have the two different fundamental unstable trigonometric modes for when $k = 5\pi/S$: $\cos(5\pi x/S)$, $\cos(3\pi x/S)\cos(4\pi x/S)$ and the superposition of the linear solutions $(\cos(5\pi x/S) + \cos(5\pi y/S))/2$. The colour bar is consistent across all images and ranges from yellow at 1 to blue at -1 (Color figure online)

or equivalently $R_c = \pi/(\sqrt{2}k_+)$. Correspondingly, the minimum area required for a square to bifurcate is $A_s = S^2 = 2R_c^2 = \pi^2/k_+^2$.

Critically, domains with symmetries will often have multiple solutions. Any solution with $m \neq n$ can have m and n swapped, providing another solution. This comes from the symmetry that any solution on the square can be rotated $\pi/2$ radians about the centre of the square and it will still be a solution due to the assumed homogeneity of the boundary conditions and that the Laplacian is rotationally invariant.

Thus, from the above discussion the fundamental solution on a square can be defined by the wave modes $(\pi/S, 0)$ and $(0, \pi/S)$, which will produce 'stripe' patterns, either horizontal or vertical, and are rotational symmetries of one another. In addition to these two solutions, there is the third solution which is a superposition of the two stripe patterns, providing a corner 'spot' pattern (see Fig. 3a).

Further, higher-order multiplicities can exist. Namely, values of k that are the same for different values of k_m and k_n, *e.g.* $(k_m, k_n) = (3\pi/S, 4\pi/S)$ will give the same k as $(k_m, k_n) = (5\pi/S, 0)$ or $(k_m, k_n) = (0, 5\pi/S)$. Moreover, any superposition of these solutions is also a solution. In Fig. 3b, we illustrate that along with the stripe solution for $k = 5$ there are also 'rhomb' and 'square' lattice spot patterns.

Enumerating the number of multiplicities requires number theory results (Hardy and Wright 1979) and is outside the scope of the current work. However, we note that, at least for the square domain, we can enumerate the multiplicity explicitly by decomposing $(kS/\pi)^2$ into its prime factors. The multiplicity of a mode then depends on the number of prime factors that are of the form $4n + 3$ where $n \in \mathbb{N}$ (see Kuttler and Sigillito 1984 for details).

This multiplicity of solutions causes the bifurcation diagram to become extremely complex as we move further from the initial bifurcation point, which is one of the reasons we are restricting our interests to the minimum bifurcation value, R_c. Equally, it is one of the reasons why Turing patterns can have defects in their arrangements on large domains; there are multiple solution modes all interacting, but none of them can dominate the full solution, thus, we end up with a superposition of modes.

5.2 Equilateral triangular domain

What follows is a manipulation of the excellent work of McCartin (McCartin 2003, 2002, 2004). For expansion on the derivation, please see the collected works in (McCartin 2011) and further properties can be found in the reviews (Grebenkov and Nguyen 2013; Kuttler and Sigillito 1984; McCartin 2008).

We, once again, consider a domain rotated from that defined in Sect. 2 as we work on an equilateral triangle that has a base length that is parallel to the horizontal and of length $S = \sqrt{3}R$. The centroid is placed at the origin (see Fig. 4a).

To construct the Laplacian on this domain, we use a triangular coordinate system (X, Y, Z) (McCartin 2002),

$$X = r - y, \tag{21}$$

$$Y = \frac{\sqrt{3}}{2}\left(x - \frac{S}{2}\right) + \frac{1}{2}(y - r), \tag{22}$$

$$Z = \frac{\sqrt{3}}{2}\left(\frac{S}{2} - x\right) + \frac{1}{2}(y - r), \tag{23}$$

where $r = R/2 = S/(2\sqrt{3})$ is the radius of the inscribed circle, (see Fig. 4b).

Since we are describing two-dimensions with three coordinates, there must be a conserved quantity and, indeed, we see that

$$X + Y + Z = 0. \tag{24}$$

Further, this coordinate system allows us to simply define and evaluate the boundary conditions as the boundaries conform to three limiting values of $X = r$, $Y = r$ and $Z = r$, respectively (see Fig. 4b) (McCartin 2002).

From (X, Y, Z), we then define the orthogonal coordinate system (ζ, η) such that $\zeta = X$ and $\eta = Y - Z$. Using the chain rule equation (11) becomes

$$\frac{\partial^2 h}{\partial x^2} + \frac{\partial^2 h}{\partial y^2} = 3\frac{\partial^2 h}{\partial \eta^2} + \frac{\partial^2 h}{\partial \zeta^2} = -k^2 h. \tag{25}$$

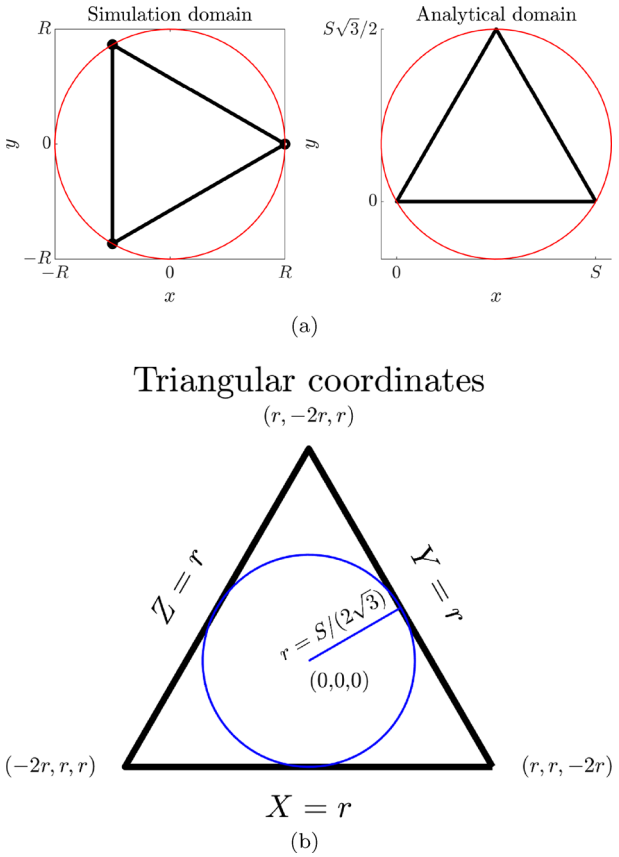

Fig. 4 **a** Rotating and translating the polygon formed by the roots unity provide the domain on which we will be algebraically deriving the Turing bifurcation point. **b** Schematic diagram illustrates the triangular coordinates (X, Y, Z)

Seeking separable solutions of the form $h(\zeta, \eta) = h_{\parallel}(\zeta)h_{\perp}(\eta)$, we must satisfy the equations

$$h_{\parallel}'' = -\alpha^2 h_{\parallel}, \tag{26}$$

$$h_{\perp}'' = -\beta^2 h_{\perp}, \tag{27}$$

which are coupled through the requirement that $k^2 = \alpha^2 + 3\beta^2$, where the positivity of the coupling constants is enforced through the requirement of trigonometric representation.

To ensure that the derivative of h is zero on $X = -2r$ and r, h will be a superposition of modes of the following form

$$h_{mn} = C_{smn}\cos\left(\frac{m\pi}{3r}(X+2r)\right)\cos\left(\beta_n(Y-Z)\right) + C_{amn}\cos\left(\frac{m\pi}{3r}(X+2r)\right)\sin\left(\beta_n(Y-Z)\right), \tag{28}$$

where $m, n \in \mathbb{N} \cup 0$ and each h_{mn} has a component that is symmetric about the triangles altitude, $Y = Z$ (the coefficient of the C_{smn} term), and a component that is antisymmetric about the triangles altitude (the coefficient of the C_{amn} term) (McCartin 2008).

Critically, to satisfy the zero-flux boundary conditions on $Y = r$ and $Z = r$, we need to restrict the possible β_n values. Specifically, it has been shown that a solution requires three symmetric terms and three antisymmetric terms, respectively (McCartin 2011),

$$\begin{aligned} h_{mn} = C_{smn}\Bigg[&\cos\left(\frac{l\pi}{3r}(X+2r)\right)\cos\left(\frac{\pi(m-n)}{9r}(Y-Z)\right) \\ &+\cos\left(\frac{m\pi}{3r}(X+2r)\right)\cos\left(\frac{\pi(n-l)}{9r}(Y-Z)\right) \\ &+\cos\left(\frac{n\pi}{3r}(X+2r)\right)\cos\left(\frac{\pi(l-m)}{9r}(Y-Z)\right)\Bigg] \\ &+C_{amn}\Bigg[\cos\left(\frac{l\pi}{3r}(X+2r)\right)\sin\left(\frac{\pi(m-n)}{9r}(Y-Z)\right) \\ &+\cos\left(\frac{m\pi}{3r}(X+2r)\right)\sin\left(\frac{\pi(n-l)}{9r}(Y-Z)\right) \\ &+\cos\left(\frac{n\pi}{3r}(X+2r)\right)\sin\left(\frac{\pi(l-m)}{9r}(Y-Z)\right)\Bigg], \end{aligned} \tag{29}$$

where $l + m + n = 0$. For simplicity, we write this as $h_{mn} = C_{smn}h_{smn} + C_{amn}h_{amn}$ where we define h_{smn} to be the symmetric terms and h_{amn} to be the antisymmetric terms.

From equation (29), the eigenvalue can be extracted,

$$\begin{aligned} k^2 &= \frac{4}{27}\left(\frac{\pi}{r}\right)^2\left(m^2+mn+n^2\right) = \frac{4}{27}\left(\frac{2\sqrt{3}\pi}{S}\right)^2\left(m^2+mn+n^2\right) \\ &= \frac{4}{27}\left(\frac{2\pi}{R}\right)^2\left(m^2+mn+n^2\right). \end{aligned} \tag{30}$$

The minimum of equation (30) occurs when $m = 1, n = 0$ (or $m = 0, n = 1$) and results in a minimum critical circumcircle radius of $R_c = 4\pi/(3\sqrt{3}k_+)$. From equation (3), we can calculate that as R increases the homogeneous steady state on a triangle bifurcates from stable to unstable at a triangle area of $A_c = 4\sqrt{3}\pi^2/(9k_+^2)$.

Note that we do not specify that A_c is the minimum triangular area that can support stable heterogeneous solutions (as we could in the square case) because, as we will see in Sect. 7, although the Turing bifurcation structure is a supercritical pitchfork on the

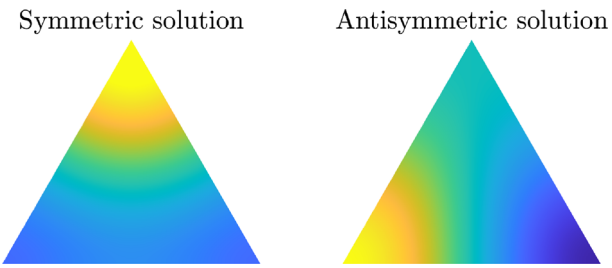

Fig. 5 Plots of the symmetric and antisymmetric eigenbases, $m = 1$, $n = 0$, $l = -1$. The images are symmetric, or antisymmetric, about the vertical altitude of the equilateral triangle. Explicitly, in the right-hand image, the bottom left corner of the triangle presents a value above zero, whereas the bottom right corner presents the same value, but negative. The value at the top of the triangle is zero. The colour axis for both images runs from blue at $-3\sqrt{3}/2$ to yellow at $3\sqrt{3}/2$ (Color figure online)

square domain (and all polygons with a higher number of edges), it has a transcritical structure on the triangular domain. Thus, on the triangular domain there is a subcritical branch of solutions that can support stable patterning solutions for area values below A_c. Hence, in the triangular case, along side deriving a numerical bifurcation point to compare against R_c, we will also numerically derive the minimum value of R for which patterns can form alongside the homogeneous steady patterns being stable.

At this point, we can compare the bifurcation circumcentre radius and polygonal areas of the triangle and square. We observe that as we increase the number of edges, we decrease the circumcentre bifurcation radius, since

$$R_{c,triangle} = \frac{4}{3\sqrt{3}}\frac{\pi}{k_+} > \frac{1}{\sqrt{2}}\frac{\pi}{k_+} = R_{c,square}. \tag{31}$$

However, the bifurcation value of the polygonal area increases

$$A_{c,triangle} = \frac{4\sqrt{3}}{9}\left(\frac{\pi}{k_+}\right)^2 < \left(\frac{\pi}{k_+}\right)^2 = A_{c,square}. \tag{32}$$

We will see later that this trend carries on for both metrics, although these values tend to limiting constants, given by the circular case, as n increases.

Before we finish this section, we once again take a look at the formula for the eigenvalues of the Laplacian on a triangular domain, equation (30) and note that its form leads to several questions that do not have obvious answers. Firstly, what numbers are representable in the form of m^2+mn+n^2? Secondly, in how many distinct ways can a given eigenvalue, k, be represented? A complete investigation into these questions and more requires the use of Eisenstein primes (Hardy and Wright 1979) and can be found in (McCartin 2011).

5.3 A note on triangular half domains

So far we have demonstrated a complete trigonometric basis for the Laplacian on a square and equilateral domain with zero-flux boundary conditions. Through this we can demonstrate that the triangular half domains, known as of the isosceles, right angled triangle (square cut along a diagonal) and the 30–60–90 triangle (equilateral triangle cut along an altitude) also have complete trigonometric bases. Further, the eigenvalues that correspond to these 'half spaces' are exactly the same as the full spaces; thus, the critical area of instability for the onset of Turing patterns (*i.e.* the smallest area for which the homogeneous steady state transitions from stable to unstable) for the isosceles, right angled triangle and the 30–60–90 triangle is exactly half that of the square and equilateral triangle, respectively.

Demonstrating this for the 30–60–90 triangle is fairly simple because, by construction, the trigonometric basis of the equilateral triangle, equation (29), is already split into terms that are symmetric and antisymmetric about an amplitude (McCartin 2004). Thus, the restriction from the equilateral triangle to the 30–60–90 triangle just requires that we use the symmetric terms,

$$\begin{aligned} h_{mn} = C_{smn} \Bigg[& \cos\left(\frac{l\pi}{3r}(X+2r)\right)\cos\left(\frac{\pi(m-n)}{9r}(Y-Z)\right) \\ & + \cos\left(\frac{m\pi}{3r}(X+2r)\right)\cos\left(\frac{\pi(n-l)}{9r}(Y-Z)\right) \\ & + \cos\left(\frac{n\pi}{3r}(X+2r)\right)\cos\left(\frac{\pi(l-m)}{9r}(Y-Z)\right)\Bigg], \end{aligned} \tag{33}$$

which have the same eigenvalues as the full equilateral triangle trigonometric basis.

To show that all solutions are of this form, we suppose there are other solutions not of this form and quickly derive a contradiction, essentially following the work of Práger (1998) using reflections and restrictions of solutions (Damle and Peterson 2010). Suppose there is a solution of the Laplacian on a 30–60–90 triangle with Neumann boundary conditions, $h_{ht}(x, y)$, $\{(x, y)|0 \le x \le S/2, 0 \le y \le \sqrt{3}x\}$, which cannot be constructed as the infinite sum of the symmetric basis elements in equation (33). Reflecting this solution along its longest altitude, we produce a symmetric solution, h_t, to the Laplacian on the equilateral domain with Neumann boundary conditions,

$$h_t(x, y) = \begin{cases} h_{ht}(x, y), & 0 \le x \le S/2, \\ h_{ht}(S-x, y), & S/2 < x \le S. \end{cases} \tag{34}$$

By construction, h_t must then have a solution in the form of an expansion made of the symmetric basis functions. Whence, by restricting h_t to the original 30–60–90 triangle domain, we recover the original solution, h_{ht}, but represented as a trigonometric sum of the basis functions, which was originally assumed not possible. By contradiction, all solutions to the Laplacian on a 30–60–90 triangle with Neumann boundary conditions can be represented as a infinite sum of the basis terms in equation (33). By extension, the eigenvalues of the equilateral triangle and the 30–60–90 triangle are the same, and

since the 30–60–90 triangle is half the area of the equilateral triangle, the minimum bifurcation area of the 30–60–90 triangle must occur at half the minimum bifurcation area of the equilateral triangle.

The case for the isosceles, right angled triangle is not so straight forward because the original solution basis, equation (20), does not have a similar split into functions that are symmetric and asymmetric across the diagonal of the square. However, we are able to use similar reflection and contraction mappings to constructively create the basis (Práger 1998; Damle and Peterson 2010).

Similar to before, suppose $h_{hs}(x, y)$ is a solution to the Laplacian on an isosceles, right angled triangle, $\{(x, y)|0 \leq y \leq S, 0 \leq x \leq S - y\}$, with Neumann boundary conditions. The reflection of h_{hs} along its hypotenuse,

$$h_s(x, y) = \begin{cases} h_{hs}(x, y), & 0 \leq x \leq S - y, \\ h_{hs}(S - y, S - x), & S - y < x \leq S, \end{cases} \tag{35}$$

produces a solution to the Laplacian on the square, $\{(x, y)|0 \leq y \leq S, 0 \leq x \leq S\}$, with Neumann boundary conditions. Further, being a reflection, the solution necessarily satisfies the Neumann boundary condition along the square's diagonal, too. Thus, $h_s(x, y)$ would have a solution form of one of the components of equation (20). By equivalently 'folding' $h_s(x, y)$ along the diagonal of the square domain, we are able to restrict $h_s(x, y)$ to be a solution of the original problem of the isosceles, right angled triangle, with Neumann boundary conditions,

$$h_{hs}(x, y) = \frac{h_s(x, y) + h_s(S - y, S - x)}{2}. \tag{36}$$

Thus, since h_s can be written as a infinite sum of $\cos(k_m x)\cos(k_n y)$ terms with eigenvalue $k = \sqrt{k_m^2 + k_n^2}$, then h_{hs} must have an equivalent form and the same eigenvalues. Explicitly, the basis elements become,

$$\begin{aligned} &\cos\left(\frac{m\pi x}{S}\right)\cos\left(\frac{n\pi y}{S}\right) + \cos\left(\frac{m\pi(S - y)}{S}\right)\cos\left(\frac{n\pi(S - x)}{S}\right) \\ &= \cos\left(\frac{m\pi x}{S}\right)\cos\left(\frac{n\pi y}{S}\right) + (-1)^{m+n}\cos\left(\frac{m\pi y}{S}\right)\cos\left(\frac{n\pi x}{S}\right). \end{aligned} \tag{37}$$

As required, we have demonstrated that the eigenfunction basis and eigenvalues of the isosceles, right angled triangle correspond to those of a square and, thus, the critical bifurcation area of a isosceles, right angled triangle is half that of the critical bifurcation area of a square.

As proven by McCartin (2008), the square and equilateral triangle are the only regular polygons that have tractable trigonometric eigenfunction bases. Thus, the isosceles, right angled triangle and the 30–60–90 triangle are the only half spaces that have tractable trigonometric eigenfunction bases.

In the next section, we consider the circle. Although we can produce an analytical basis for the circle case the corresponding eigenvectors do not have simple closed-form expression, although we are able to make headway using numerics and approximations.

5.4 Circular domain

The natural coordinate system for a circular domain is the cylindrical polars, $(x, y) = (\rho\cos(\theta), \rho\sin(\theta))$, where $\rho \in (0, R)$ and $\theta \in [0, 2\pi)$. Under this coordinate change equation (11) becomes

$$\nabla^2 h = \frac{1}{\rho}\frac{\partial}{\partial\rho}\left(\rho\frac{\partial h}{\partial\rho}\right) + \frac{1}{\rho^2}\frac{\partial^2 h}{\partial\theta^2}. \tag{38}$$

Assuming a separable solution, we can solve the Laplacian using a solution of the form $h = B(\rho)\Theta(\theta)$, where Θ is 2π periodic and B satisfies the Neumann boundary condition, $B'(R) = 0$. Further, B and Θ are assumed to be finite everywhere. Substituting the separable form into equation (11) gives

$$B''\Theta + \frac{1}{\rho}B'\Theta + \frac{1}{\rho^2}B\Theta'' = -k^2 B\Theta, \tag{39}$$

where the primes denote derivatives with the respective variables. Dividing through by $B\Theta/\rho^2$ allows us to decouple the ρ and θ variables,

$$\underbrace{\frac{B''\rho^2}{B} + \frac{B'\rho}{B} + \rho^2 k^2}_{\substack{\text{Function of } \rho \\ \text{only}}} = \underbrace{-\frac{\Theta''}{\Theta}}_{\substack{\text{Function of } \theta \\ \text{only}}} = \underbrace{p^2}_{\substack{\text{Function of} \\ \text{neither } \rho \text{ or } \theta}}. \tag{40}$$

From equation (40) and the desired periodic features, we can show that Θ must have the form

$$\Theta(\theta) = a\cos(p\theta) + b\sin(p\theta) = c\cos(p\theta + \phi), \tag{41}$$

where $p \in \mathbb{N} \cup 0$ for Θ to be periodic 2π. The constants a and b are defined by the initial conditions and can be written in the condensed form using c and ϕ. Since the equations are invariant under rotation, then through judicious rotation of the final solution we can fix $\phi = 0$.

The equation for B can be rearranged to

$$B''\rho^2 + B'\rho + (\rho^2 k^2 - p^2)B = 0 \tag{42}$$

which is a scaled version of Bessel's differential equation (Khosravian-Arab et al. 2017). Although there are two families of solutions to this equation, only one of these families is finite at $\rho = 0$. Thus, the solution of equation (42) is $B_p(k\rho)$, where B_p is a Bessel function of the first kind of order p and k is defined by the satisfying the boundary condition, $B_p'(kR) = 0$.

Critically, the values of k do not have a simple form, compared to the frequencies in the square and triangle case (see Fig. 6a). However, we will be most interested in the first unstable frequency, namely the smallest nonzero value of kR which allows a spatially heterogeneous solution to exist. Values of kR for the first five values of p are presented in Table 1 and Fig. 6b.

Table 1 The value of $kR > 0$ at which $B_p(kR)$ has its first zero derivative for different values of p

p	0	1	2	3	4
kR to 2 d.p	3.83	1.84	3.05	4.20	5.32

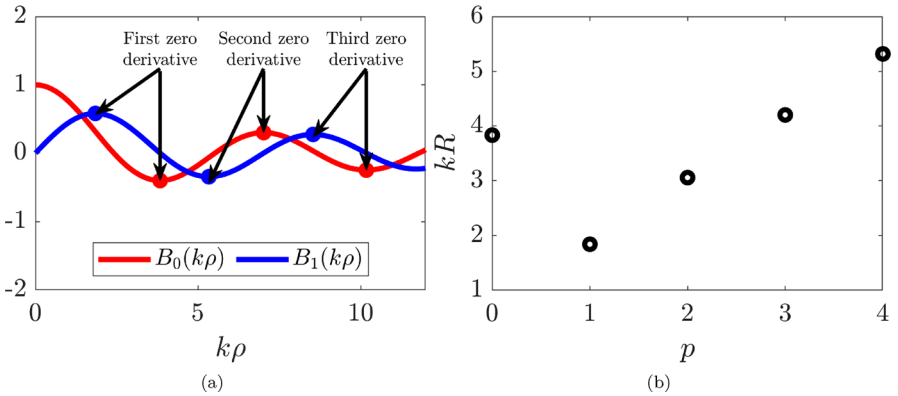

Fig. 6 Illustrating the zero derivatives of the Bessel functions. **a** First two Bessel functions of the first type for $k\rho \in [0, 12]$. The first three zero derivatives with $k\rho > 0$ are highlighted as circles. Note that the values of $k\rho$ for the zero derivatives of B_1 are always smaller than their analogues of B_0. **b** The value of the first zero derivative for Bessel functions of order $p = 0, \ldots, 4$. For $p \geq 1$, the values increase monotonically

We note that, unlike the frequencies in the square and triangle cases, these do not form a monotonically increasing sequence. Since k_+ is fixed by the kinetics and diffusion parameters, this means that a growing circle will first reach the bifurcation value set by $p = 1$ before $p = 0$.

Further, in the polar case although we have used a solution form that is separable in the coordinates, the two functions are inextricably linked through p as

$$h = cB_p(k\rho)\cos(p\theta). \tag{43}$$

This is in contrast to the square domain case, where the frequency in the x- and y-directions can be altered independently (see equation (20)).

The first three eigenmodes are illustrated in Fig. 7. We note that even though the eigenbases (Eq. (43)) are more complicated that the trigonometric solutions, the cascade of patterns to which we can bifurcate to are consistent across the regular shapes. Namely, the first bifurcation will be to a striped pattern ($p = 1$), and then, edge spots are able to occur ($p = 2$), before centralised spots are able to form for larger areas ($p = 0$).

Although the zeros of the Bessel function and its derivatives do not have a simple form, there has been much analytical work deriving bounds on their values, as well as providing approximations for the zeros (Elbert 1991; Giordano and Laforgia 1983; Maass and Martin 2018; Watson 1918; Baricz et al. 2018). Since we are looking for the first zero, we are able to derive a good approximation from using the first few terms in the Bessel function's power series expansion (Morgenthaler and Reismann 1963;

Fig. 7 Illustrations of equation (43) for $p = 0$, 1 and 2. $\rho \in [0, R]$ and the $k > 0$ value depends on p and is defined by $B_p'(kR) = 0$, see text, Table 1 and Fig. 6a for details. The colour axis in all cases is fixed to be blue at -1 and yellow at 1 (Color figure online)

Harrison 2009). Namely, for nonnegative integer, p,

$$B_p(x) = \sum_{n=0}^{\infty} \frac{(-1)^n}{n!(n+p)!} \left(\frac{x}{2}\right)^{2n+p}. \tag{44}$$

As discussed above, the smallest value of kR to become unstable will be the solution to $B_1'(k_+R_c) = 0$. The quartic order approximation to this value is

$$B_1'(x) \approx \frac{1}{2} - \frac{3}{16}x^2 + \frac{5}{384}x^4. \tag{45}$$

Since this is a quadratic in x^2, it is trivially solvable, providing four roots of the form

$$k_+R_c = \pm\frac{2}{5}\sqrt{45 \pm 5\sqrt{21}}, \tag{46}$$

where all sign combinations are used. The approximate solution we derive is then $k_+R_c = 0.4\sqrt{45 - 5\sqrt{21}} \approx 1.88$, to 2 d.p., which we can be compared it to the tabulated value of $k_+R_c \approx 1.84$.

Extending the power series allows us to become more accurate, and at the next order, the approximate equation would be cubic in x^2, which again is solvable by radicals and provides a solution correct to 2 d.p.. However, the accuracy provided by the quadratic equation solution is good enough to show that once again the critical area is larger than that of the square. Specifically,

$$\begin{aligned} A_{c,circle} &= \pi R_{c,circle}^2 > \pi \left(\frac{1.8}{k_+}\right)^2 \\ &= \frac{1.8^2}{\pi}\left(\frac{\pi}{k_+}\right)^2 > 1.03\left(\frac{\pi}{k_+}\right)^2 > A_{c,square} > A_{c,triangle}, \end{aligned} \tag{47}$$

whilst direct calculation confirms that $R_{c,circle} < R_{c,square} < R_{c,triangle}$. Hence, we have analytically shown that if we consider growing shapes of equal area, then the triangle will bifurcate to patterns first, followed by the square and then the circle following shortly behind. Based on this trend, we can hypothesise that the smallest

bifurcation areas of all other polygons will lie in the interval set by the triangle and circle, whilst also conjecturing that as the number of edges increases, the smallest bifurcation area increases, but the radius of the polygon's circumcentre will decrease. These relations will be confirmed in Sect. 7.

6 Nonlinear analysis

At this point, we could simulate the systems and derive the bifurcation points to compare against the analysis in the previous chapter. However, we will be going further than this as we are able to follow the unstable and stable branches of the solution bifurcations. As we will see in Sect. 7, this leads to an unexpected result; namely, on a square (or rectangular) domain with zero-flux boundary conditions we expect the bifurcation structure to be of a pitchfork style, either supercritical or subcritical. (Leppänen 2004; Benson et al. 1998; Crampin 2000; Dutt 2010, 2012; Grindrod 1996; Nicolis 1995; Auchmuty and Nicolis 1975; Bozzini et al. 2015; Breña-Medina and Champneys 2014; Dalwadi and Pearce 2022). Thus, we may expect such a bifurcation structure on all polygonal domains and this is certainly what is observed for polygons with larger numbers of edges. However, for the triangle, we will see that the bifurcation is actually a transcritical bifurcation.

Since we are able to generate a trigonometric basis for the square and triangle geometries, we can push our investigation further beyond linear analysis to weakly nonlinear analysis and derive the bifurcation structure. Specifically, we are going to expand our solutions about the Turing bifurcation point with smallest circumcentre radius, R_c. This restriction to the first bifurcation point reduces the number of possible solutions that will appear and is one of the primary assumptions that will enable progress (Schneider and Uecker 2017; Uecker et al. 2014; Nicolis 1995; Olver 2014).

Weakly nonlinear analysis depends on the use of an ansatz expansion. Thus, it is not always applicable (Leppänen 2004; Benson et al. 1998; Crampin 2000; Dutt 2010, 2012; Barrass et al. 2006; Grindrod 1996; Nicolis 1995; Auchmuty and Nicolis 1975; Bozzini et al. 2015; Wollkind et al. 1994). However, the theory presented in this section is backed up by intuition built on simulations and numerically derived bifurcation structures. Equally, we will demonstrate a posteriori that our final algebraic derivations match the simulated structures.

Another assumption regarding our approach is that we assume that the bifurcations branches emerge from $R = R_c$ in a connected and continuous manner. We are unable to identify bifurcation points (analytically, or numerically) if they are not connected via the homogeneous solution branch, as this is the solution about which we are perturbing. There are deflation techniques which are numerically able to identify such isolated bifurcation branches. However, we have never observed such isolated branches and the simulated bifurcation branches produce all patterns that we have simulated. Thus, we assume that such branches either do not exist or are rare enough to not influence our approach.

As in Sect. 4, we cover the general theory before specifying to the particular domains. Once again, we begin with applying our techniques to the square domain,

which the reader may be more familiar with. Then, we adapt the techniques to the triangular domain.

Since we are using the spatial scale as the bifurcation parameter, it is easier to work with if we non-dimensionalise the length scale as $(x, y) = (Sx', Sy')$. This draws out the dependency of the bifurcation parameter out into the Laplacian,

$$\nabla^2_{(x,y)} = \frac{\partial^2}{\partial x^2} + \frac{\partial^2}{\partial y^2} = \frac{1}{S^2}\left(\frac{\partial^2}{\partial x'^2} + \frac{\partial^2}{\partial y'^2}\right) = \frac{1}{S^2}\nabla^2_{(x',y')} \tag{48}$$

We can then perturb around the bifurcation point $S = S_c$, (or equivalently $R = R_c$), in terms of a power series of $0 < \epsilon \ll 1$.

This ϵ is not the same as the ϵ_u and ϵ_v used previously. In Sect. 5.1, ϵ_u and ϵ_u were undefined small perturbations that included the amplitude dependencies. We now separate the small perturbation from the amplitude function as it is this function's dependency on the kinetics that we are going to derive.

We also expand the solution, $\boldsymbol{u}$, and the time dependency using ϵ. The solution is expanded because of the assumption that it varies continuously on the value of S. The time dependency is expanded because we assume that close to S_c the full system is close to steady state and, thus, convergence to the steady state is slow, which requires new multiscale time variables to be included (Nicolis 1995; Stanley 1987). Overall the expansions are

$$S = S_c + \epsilon S_1 + \epsilon^2 S_2 + \ldots, \tag{49}$$

$$\frac{\partial}{\partial t} = \epsilon\frac{\partial}{\partial t_1} + \epsilon^2\frac{\partial}{\partial t_2} + \ldots, \tag{50}$$

$$\boldsymbol{u}(\boldsymbol{x}', t_1, t_2) = \begin{pmatrix} u_s \\ v_s \end{pmatrix} + \epsilon \boldsymbol{U}_1(\boldsymbol{x}', t_1, t_2) + \epsilon^2 \boldsymbol{U}_2(\boldsymbol{x}', t_1, t_2) + \ldots, \tag{51}$$

Substituting equations (49)-(51) into system equations (4) and (5) (with the rescaled Laplacian) and expanding in terms of ϵ allow us to collect the differing orders of ϵ into the following cascade of equations:

$$\mathcal{O}(\epsilon) \quad \boldsymbol{\mathcal{L}}\boldsymbol{U}_1 = 0, \tag{52}$$

$$\mathcal{O}(\epsilon^2) \quad \boldsymbol{\mathcal{L}}\boldsymbol{U}_2 = \frac{\partial \boldsymbol{U}_1}{\partial t_1} + \frac{2S_1}{S_c^3}\boldsymbol{D}\nabla_{(x',y')}\boldsymbol{U}_1 - \frac{U_1^2}{2}\begin{pmatrix} f_{uu} \\ g_{vv} \end{pmatrix} - U_1 V_1 \begin{pmatrix} f_{uv} \\ g_{uv} \end{pmatrix} - \frac{V_1^2}{2}\begin{pmatrix} f_{vv} \\ g_{vv} \end{pmatrix}, \tag{53}$$

$$\mathcal{O}(\epsilon^3) \quad \boldsymbol{\mathcal{L}}\boldsymbol{U}_3 = \frac{\partial \boldsymbol{U}_1}{\partial t_2} + \frac{\partial \boldsymbol{U}_2}{\partial t_1} - \left(\frac{3S_1^2 - 2S_2 S_c}{{S_c}^4}\right)\boldsymbol{D}\nabla_{(x',y')}\boldsymbol{U}_1 + \frac{2S_1}{S_c^3}\boldsymbol{D}\nabla_{(x',y')}\boldsymbol{U}_2$$

$$
\begin{aligned}
&- \begin{pmatrix} f_{uu}U_1 + f_{uv}V_1 & f_{uv}U_1 + f_{vv}V_1 \\ g_{uu}U_1 + g_{uv}V_1 & g_{uv}U_1 + g_{vv}V_1 \end{pmatrix} \boldsymbol{U}_2 \\
&- \frac{1}{6} \begin{pmatrix} f_{uuu}U_1^3 + f_{vvv}V_1^3 \\ g_{uuu}U_1^3 + g_{vvv}V_1^3 \end{pmatrix} - \frac{U_1 V_1}{2} \begin{pmatrix} f_{uuv} & f_{uvv} \\ g_{uuv} & g_{uvv} \end{pmatrix} \boldsymbol{U}_1,
\end{aligned} \tag{54}
$$

where $\boldsymbol{\mathcal{L}}$ is the linear operator

$$
\boldsymbol{\mathcal{L}} = \frac{1}{S_c^2} \boldsymbol{D} \nabla_{(x',y')} + \boldsymbol{J}. \tag{55}
$$

Although we can expand the system up to any order in ϵ, we will find that the amplitude equations are defined at the third order for the square domain and the second order for the triangular domain.

6.1 Square domain

Due to the spatial non-dimensionalisation, we are now working on the square $[0, 1] \times [0, 1]$. We have effectively already solved equation (52) in Sect. 5.1 as we are looking for a null vector of equation (55) near the first bifurcation point. Up to a multiplicative constant and symmetry of swapping x' and y', the solution is

$$
\boldsymbol{U}_1 = \begin{pmatrix} \Lambda \\ 1 \end{pmatrix} \left(a(t_1, t_2) \cos(\pi x') + b(t_1, t_2) \cos(\pi y') \right), \tag{56}
$$

Note that we used the freedom of the multiplicative constant to normalise the coefficient of the v amplitude in equation (56). Using this form, we can derive that Λ satisfies

$$
0 = -\frac{D_u \pi^2}{S_c^2} \Lambda + \Lambda f_u + f_v \implies \Lambda = \frac{f_v S_c^2}{D_u \pi^2 - S_c^2 f_u}. \tag{57}
$$

Since a nontrivial value of $\boldsymbol{U}_1$ exists, $\mathcal{L}$ has a nontrivial kernel, and therefore, the adjoint operator, $\mathcal{L}^T$, also has a nontrivial kernel. In the case, we are considering the adjoint operator is simply the transposition of the matrix corresponding to $\mathcal{L}$, hence the naming convention. The basis of $\mathrm{Ker}\left(\mathcal{L}^T\right)$ is spanned by the two solutions of

$$
\mathcal{L}^T \boldsymbol{W} = 0, \tag{58}
$$

which are multiples of

$$
\boldsymbol{W}_1 = \begin{pmatrix} \Gamma \\ 1 \end{pmatrix} \cos(\pi x'), \text{ and } \boldsymbol{W}_2 = \begin{pmatrix} \Gamma \\ 1 \end{pmatrix} \cos(\pi y') \tag{59}
$$

where

$$
\Gamma = \frac{g_u S_c^2}{D_u \pi^2 - S_c^2 f_u}. \tag{60}
$$

In order for each of the equations in the expansion cascade to have a solution, the solution must satisfy that the right-hand side of the equations must be perpendicular to all solution in Ker $\left(\mathcal{L}^T\right)$ (Ramm 2001), where, by perpendicular, we mean equal to zero under the following inner product

$$\langle \boldsymbol{h}_1, \boldsymbol{h}_2 \rangle = \int_0^1 \int_0^1 \boldsymbol{h}_1(x', y') \cdot \boldsymbol{h}_2(x', y') \, \mathrm{d}x' \, \mathrm{d}y', \tag{61}$$

where the dot symbolises the normal vector dot product, or component-wise multiplication.

The right-hand side of equation (52) is trivially perpendicular to all vectors. So, we now consider the right-hand side of equation (53). Critically, apart from the spatial and temporal derivative terms the rest of the solution will be made up of quadratic terms in $\cos(\pi x')$ and $\cos(\pi y')$. Due to standard properties of Fourier series (Kreyszig 2007), we know that superposition solutions of $\cos(\pi x')$ and $\cos(\pi y')$ will be perpendicular to their quadratic counterparts. Thus, if we assume there is no t_1 dependence in the solution and $S_1 = 0$, we can guarantee that the equation (53) can be solved. However, this does mean that we do not gain any restrictions on the amplitude equations $a(t_1, t_2)$ and $b(t_1, t_2)$ from equation (56) and, thus, we must head to the third order expansion, equation (54).

Having solved equation (53) for $\boldsymbol{U}_2$ (explicit solution can be found in Appendix A), we can then substitute $\boldsymbol{U}_1$ and $\boldsymbol{U}_2$ into equation (54). From this substitution, we will see that the right-hand side of equation (54) will have terms that are not naturally orthogonal to equation (59). Thus, we use Fredholm's alternative theorem to enforce that any nonzero coefficients sum together to zero, which will remove secular, or resonant, terms (Ramm 2001). The solvability criteria is then

$$\langle \boldsymbol{W}_1, \mathcal{L}\boldsymbol{U}_3 \rangle = 0, \text{ and } \langle \boldsymbol{W}_2, \mathcal{L}\boldsymbol{U}_3 \rangle = 0. \tag{62}$$

Criteria (62) are given explicitly in Appendix A; however, upon rearrangement we can specify that a and b satisfy equations of the form

$$\frac{\mathrm{d}a}{\mathrm{d}t_2} = p_1 a^3 + (b^2 p_2 + S_2 p_3) a, \tag{63}$$

$$\frac{\mathrm{d}b}{\mathrm{d}t_2} = p_1 b^3 + (a^2 p_2 + S_2 p_3) b, \tag{64}$$

where the form and signs of p_1, p_2 and p_3 are given by the kinetic and diffusion parameters. The parameter S_2 represents how far from the bifurcation point we are and whether we are above ($S_2 > 0$) or below ($S_2 < 0$) the bifurcation value.

There are nine steady-state solutions, (a_s, b_s), of equations (63) and (64), and these are:

1. the homogeneous steady state, $(0, 0)$;
2. stripe patterns, $(\pm a_1, 0)$, $(0, \pm b_1)$;
3. spot patterns, $(a_2, \pm a_2)$, $(\pm a_2, a_2)$;

where $a_1 = b_1 = \sqrt{-p_3 S_2/p_1}$ and $a_2 = \sqrt{-p_3 S_2/(p_1 + p_2)}$. The plus and minus signs then account for the solution symmetries on the square. Thus, up to symmetry, there are only three distinct solutions, the homogeneous steady state, $(0, 0)$: a stripe, $(a_1, 0)$, and a spot (a_2, a_2).

To make further progress, we consider a simple ODE linear stability analysis about each of the steady states. The eigenvalues of the Jacobian of equations (63) and (64) at steady state are

1. the homogeneous steady state, $\lambda_{1,2} = p_3 S_2$;
2. stripe patterns, $\lambda_1 = -2p_3 S_2$, $\lambda_2 = p_3 S_2(p_1 - p_2)/p_1)$;
3. spot patterns, $\lambda_1 = -2p_3 S_2$, $\lambda_2 = 2p_3 S_2(p_2 - p_1)/(p_1 + p_2)$;

Since the homogeneous steady state is stable for $S_2 < 0$ and unstable for $S_2 > 0$ then would must have that $p_3 > 0$. The signs of p_1 and p_2 then specify whether the solutions bifurcate supercritically or subcritically. Since we want supercritical bifurcations, then the stripe solutions tell us that we want $p_1 < 0$ and the spot solution tell us we need $p_1 + p_2 < 0$. Since p_1, $p_1 + p_2 < 0$, then the signs of the eigenvalues of the stripe and spot solutions depend on the sign of $p_1 - p_2$. However, whatever sign $p_1 - p_2$ takes the eigenvalues that depend on $p_1 - p_2$ take opposite signs in the two different cases. Thus, exactly one of the spot or stripe solutions bifurcates in a stable manner from R_c, whilst the other bifurcates in an unstable manner.

Later, in Sect. 7 we will present the exact values of p_1, p_2 and p_3 in the case of the Schnakenberg kinetics. We will demonstrate that the maxima and minima of the solutions derived from simulations closely match the weakly nonlinear analysis, at least close to the bifurcation point. Further, we will show that the stability characteristics and bifurcation structures are as specified from the above analysis

6.2 Equilateral triangular domain

The approach to extracting the bifurcation structure based on a triangular domain is similar to that shown in Sect. 6.1. However, there are some subtleties that we first highlight. Critically, the intuition for the following analysis was gained after simulation; thus, the interested reader may wish to view Sect. 7 before delving into the algebraic derivation.

In the square domain case, we observed that the solution could bifurcate into a stripe, or corner spot (see Fig. 3), providing two families of different solutions. Such a categorisation does not extend to the triangle, because on a triangular domain a stripe that is parallel to one side naturally produces a corner spot in the opposite corner (see the left-hand figure of Fig. 5).

The split of the solutions into symmetric and antisymmetric parts naturally produces two alternative families of solutions. However, when the bifurcation structures were simulated, there appeared to be no bifurcation branch stemming from the homogeneous solution that followed the antisymmetric solutions, at least initially.

The weakly nonlinear analysis allows us to understand why this is so. Namely, we are going to show that the solubility criterion for the triangular domain occurs at the second order expansion, equation (53) (rather than the third order expansion, equation (54), which was required for the square domain). This means that the Turing

bifurcation on the triangle domain is generically transcritical. Furthermore, this also means that we cannot bifurcate to antisymmetric solutions. The reason why stems from the form of the right-hand side of equation (53). Namely, all of the solution functions are quadratic, but if you multiply an antisymmetric solution by scaled version of the same antisymmetric solution you generate a symmetric solution. Thus, if we were to run the weakly nonlinear analysis trying to find antisymmetric solution forms, we would quickly find that we would not be able to solve equation (53) because the left-hand side would be antisymmetric, whereas the right-hand side would be symmetric.

Now, this argument only works for purely antisymmetric solutions. If we were to consider a superposition solution, then it is possible not only to solve, equation (53), but also derive the solvability criterion. Specifically, consider the superposition solution

$$\boldsymbol{U}_1 = \begin{pmatrix} \Lambda \\ 1 \end{pmatrix} (a(t_1)h_{s10} + b(t_1)h_{a10}). \tag{65}$$

where $a(t_1)$ and $b(t_1)$ are the amplitude equations. Then by the Fredholm alternative theorem, the right-hand side of equation (53) must be perpendicular to both

$$\boldsymbol{W}_s = \begin{pmatrix} \Gamma \\ 1 \end{pmatrix} h_{s10}, \text{ and } \boldsymbol{W}_a = \begin{pmatrix} \Gamma \\ 1 \end{pmatrix} h_{a10}, \tag{66}$$

where the inner product on the triangular domain is

$$\langle \boldsymbol{h}_1, \boldsymbol{h}_2 \rangle = \int_0^{\sqrt{3}/2} \int_{y'/\sqrt{3}}^{(\sqrt{3}-y')/\sqrt{3}} \boldsymbol{h}_1(x', y') \cdot \boldsymbol{h}_2(x', y') \, \mathrm{d}x' \, \mathrm{d}y'. \tag{67}$$

The solubility criteria is, thus, two coupled ODEs for the amplitudes $a(t_1)$ and $b(t_1)$

$$\begin{aligned} 0 = &- \frac{\left((\eta f_{uu} + g_{uu})\,\Lambda^2 + (2\eta f_{uv} + 2g_{uv})\,\Lambda + f_{vv}\eta + g_{vv}\right) 3a^2}{16} \\ &- \frac{4\pi^2 S_1\,(\Lambda D_u \eta + D_v)\,a}{3{S_c}^3} \\ &+ \frac{\left((\eta f_{uu} + g_{uu})\,\Lambda^2 + (2\eta f_{uv} + 2g_{uv})\,\Lambda + f_{vv}\eta + g_{vv}\right) 3b^2}{16} + \frac{3\,(\eta\Lambda + 1)}{8}\frac{\mathrm{d}a}{\mathrm{d}t_1}, \\ 0 = &\frac{\left((\eta f_{uu} + g_{uu})\,\Lambda^2 + (2\eta f_{uv} + 2g_{uv})\,\Lambda + f_{vv}\eta + g_{vv}\right) 3ba}{8} \\ &- \frac{4\pi^2 S_1\,(\Lambda D_u \eta + D_v)\,b}{3{S_c}^3} + \frac{3\,(\eta\Lambda + 1)}{8}\frac{\mathrm{d}b}{\mathrm{d}t_1}, \end{aligned}$$

which can be written in the simplified form

$$\frac{\mathrm{d}a}{\mathrm{d}t_1} = p_1(b^2 - a^2) + S_1 p_2 a, \tag{68}$$

$$\frac{\mathrm{d}b}{\mathrm{d}t_1} = (2p_1 a + S_1 p_2)b, \tag{69}$$

where p_1 and p_2 are appropriately defined. The system of equations (68) and (69) are then susceptible to standard ODE analysis. There are four steady states,

$$(0,0), \quad \left(\frac{p_2 S_1}{p_1}, 0\right), \quad \left(-\frac{S_1 p_2}{2p_1}, \pm\frac{\sqrt{3}}{2}\frac{S_1 p_2}{p_1}\right), \tag{70}$$

These correspond to the homogeneous steady state, symmetric heterogeneous solutions and superposition solutions. Since we know that $(0, 0)$ must be stable for $S_1 < 0$, a simple linear stability analysis argument allows us to deduce that $p_2 > 0$. Further, for all steady states the stability does not depend on p_1 and the patterned solution steady states are all saddle points for all values of $S_1 \neq 0$.

Thus, as we will see in Sect. 7, due to the transcritical nature of the bifurcation structure that are heterogeneous solution branches that bifurcate into both regions of $S_1 < 0$ and $S_1 > 0$. However, all branches are unstable. Of course this result is misleading as it depends only on weakly nonlinear analysis, which is only valid close to $S = S_c$. What we will observe is that both branches do transition to produce stable patterns. Specifically, the subcritical branch stabilises for $S < S_c$ and continues to be stable for $S > S_c$; thus, stable heterogeneous solutions do exist for $S > S_c$.

To provide further information on the bifurcation diagram and generate a solution that would demonstrate where and when the branches transition to stability, we could perhaps go to the third order ϵ expansion, or even higher. However, because the stability transitions do not occur close to the bifurcation point, it is likely that higher-order expansions will not generate the required solutions and potentially lead to inaccurate insights (Bozzini et al. 2015; Becherer et al. 2009). Thus, we leave the theory here and in the next section apply the theory to a particular set of Turing kinetics and demonstrate that although our theory is correct, we need numerical simulations to fill in details far away from the bifurcation point.

7 Results

To derive the bifurcation diagrams, we will use a numerical bifurcation package, `pde2path`, version 3.0 (Uecker et al. 2014; Dohnal et al. 2014; Uecker 2021; Engelnkemper et al. 2019). The evidence provided by `pde2path` is then supported by independent simulations, completed using COMSOL Multiphysics 5.1 (Multiphysics 2021). All of the following simulation script and files can be found at https://github.com/ThomasEWoolley/Tractable_Turing_patterns. Each script contains details regarding the technical aspects of the simulation, *e.g.* spatial discretisation, iteration tolerance, etc. Although all tolerances and discretisations were pushed to their computational limits of accuracy, our final chosen parameters were picked to allow efficient parameter sweeps over multiple geometries, whilst maintaining accuracy through generating simulations that are not dependent on the parameters of the solution method.

7.1 Linear analysis of the Schnakenberg kinetics

We will be using the Schnakenberg system to illustrate the derived theory (Gierer and Meinhardt 1972; Schnakenberg 1979). It is a well-known set of kinetics that produce Turing patterns over a wide range of parameter values. Moreover, it is known that the bifurcation structure of the Schnakenberg system on a square domain is a supercritical pitchfork (Woolley 2022). For demonstrative purposes, we fix all parameter values, apart the radius of the circumcircle, R, in which we prescribe the polygon. As far as we have seen from simulations, the theory holds for all tested parameter values. The ones we choose here simply provide 'nice' values for the derivable bifurcation points. The explicit form we are going to deal with is

$$\frac{\partial u}{\partial t} = \nabla^2 u + \frac{1}{10} - u + u^2 v, \tag{71}$$

$$\frac{\partial v}{\partial t} = 10\nabla^2 v + \frac{9}{10} - u^2 v. \tag{72}$$

The boundary conditions are zero-flux on all polygonal boundaries. The initial condition (when simulating time dependent simulations) is random noise about the steady state of $(u_s, v_s) = (1, 9/10)$. The Jacobian is

$$\boldsymbol{J}(u_s, v_s) = \begin{pmatrix} 2u_s v_s - 1 & u_s^2 \\ -2u_s v_s & -u_s^2 \end{pmatrix} = \begin{pmatrix} 4/5 & 1 \\ -9/5 & -1 \end{pmatrix}, \tag{73}$$

and the Hessians of f and g are

$$\boldsymbol{H}_f(u_s, v_s) = \begin{pmatrix} f_{uu} & f_{uv} \\ f_{vu} & f_{vv} \end{pmatrix} = \begin{pmatrix} 2v & 2u \\ 2u & 0 \end{pmatrix} = \begin{pmatrix} 9/5 & 2 \\ 2 & 0 \end{pmatrix}, \quad \boldsymbol{H}_g(u_s, v_s) = \begin{pmatrix} g_{uu} & g_{uv} \\ g_{vu} & g_{vv} \end{pmatrix} = \begin{pmatrix} -2v & -2u \\ -2u & 0 \end{pmatrix} = \begin{pmatrix} -9/5 & -2 \\ -2 & 0 \end{pmatrix}.$$

From these, we can check that the trace and determinant of $\boldsymbol{J}$ are negative and positive, respectively, and, thus, the steady state is stable in the absence of diffusion. Diffusion is then able to drive the system to instability if there exists some k, for which $Det(\boldsymbol{J} - k^2\boldsymbol{D}) < 0$. From solving equation (15), this is true for $k_-^2 = 1/5 < k^2 < 1/2 = k_+^2$.

Having calculated k_+, we can explicitly define the smallest critical size of the equilateral triangle, square and circle that allow the homogeneous steady state to destabilise. These algebraic and calculated values are collected in Table 2.

We evidence the bifurcation boundaries listed in Table 2 in Fig. 8, where we simulate equations (71) and (72) on the equilateral triangle, square and circular domains of different sizes. Specifically, we pick values of R where no patterns should exist ($R = 2.5$, top of Fig. 8) and then about each of the critical values denoted in the R_c row of Table 2. Clearly, we observe from top to bottom of Fig. 8 that as the area of the polygon increases, the bifurcation cascade follows the order set out in Table 2, namely the circle patterns first, then the square and, finally, the triangle.

Table 2 Bifurcation points marking the transition from stable homogeneous steady state to unstable homogeneous steady state

Geometry	Equilateral triangle	Square	Circle
Circumcircle radius bifurcation value, R_c	$\frac{4}{3\sqrt{3}}\frac{\pi}{k_+} = \frac{4\sqrt{2}}{3\sqrt{3}}\pi = 3.42$	$\frac{\pi}{\sqrt{2}k_+} = \pi = 3.14$	$\frac{1.84}{k_+} = 1.84\sqrt{2} = 2.60$
Polygon side length bifurcation value, S_c	$\frac{4\pi}{3k_+} = \frac{4\sqrt{2}}{3}\pi = 5.92$	$\frac{\pi}{k_+} = \sqrt{2}\pi = 4.44$	
Shape area bifurcation value, A_c	$\frac{4\sqrt{3}}{9}\left(\frac{\pi}{k_+}\right)^2 = \frac{8\sqrt{3}}{9}\pi^2 = 15.20$	$\left(\frac{\pi}{k_+}\right)^2 = 2\pi^2 = 19.74$	$\frac{\pi 1.84^2}{k_+^2} = 6.77\pi = 21.30$

In each case, the general algebraic form is noted with the corresponding exact value and numerical value to 2 d.p. that follows from equations (71) and (72). Note that R_c, S_c and A_c are related via equations (2) and (3). Further, note there is no S_c value in the case of the circle because the circle has no nontrivial edges

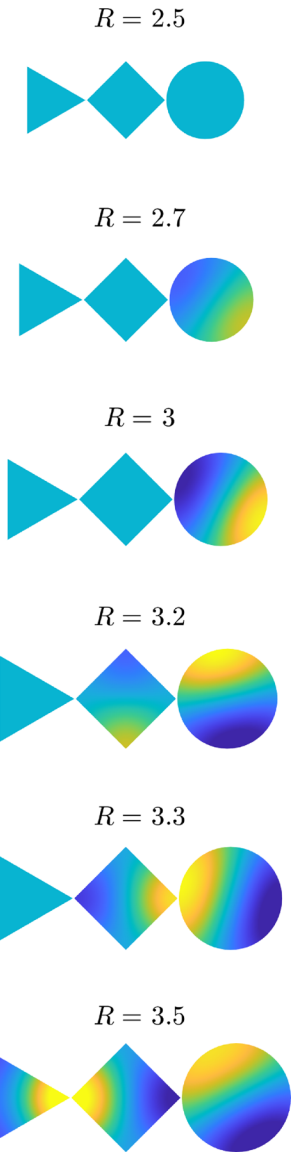

Fig. 8 Simulations of equations (71) and (72) on the equilateral triangle, square and circular domains of different sizes. The radius of the circumcentre, R, for each row of polygons is given above each figure. The colour bar over all figures is fixed from -0.6 (blue) to 1.5 (yellow). Each simulation is run for 10^4 units, after which no further transitions where observed (Color figure online)

Alongside Table 2, Fig. 9 fills in the bifurcation points for R_c and A_c for all other polygons that do not have tractable eigenbases. Specifically, it was constructed using the numerical software `pde2path` and provides the smallest value of R_c, or A_c, at which the homogeneous steady state destabilises (blue circles). For the equilateral triangle ($n = 3$) and square cases ($n = 4$), we compare the numerically derived values with the algebraically derived values, collated in Table 2 (black diamonds). Clearly, there is excellent correspondence. Further, as hypothesised in Sect. 5, we see that as the number of edges of the polygon increases, the circumcentre radius bifurcation

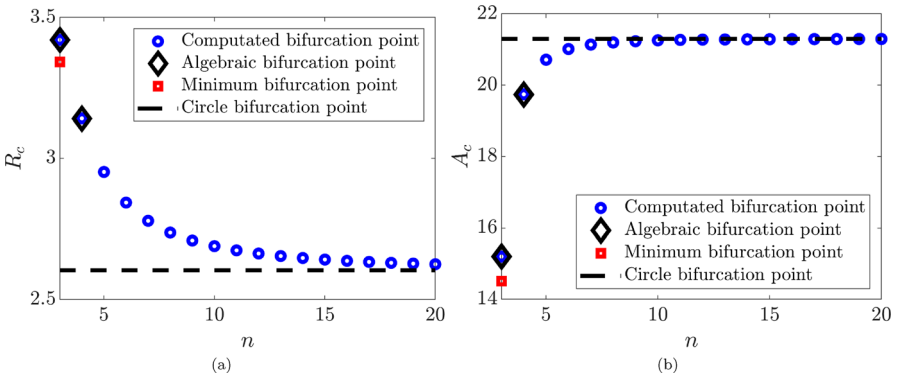

Fig. 9 Deriving the smallest bifurcation values of the circumcentre (left) and area (right) for which the homogeneous steady-state solution of equations (71) and (72) destabilises. Alongside the computed values (blue circles), we compare the analytically derived estimates of the equilateral triangle, square (black diamonds) and circle (dashed line asymptote). The red square is the numerically derived bifurcation point on the subcritical patterning branch that generates stable patterns (Color figure online)

point monotonically decreases, whilst the bifurcation area monotonically increases. In both cases, the curves asymptote at the values derived for the circular domain case (black dashed line).

7.2 Weakly nonlinear analysis of the Schnakenberg kinetics

As we evidenced in Sect. 6, the bifurcation structure on the triangle domain is transcritical. This means that it is possible to have pattern states that are stable for values of $R < R_c$. Indeed, this will be shown later. Thus, the red square data points in Fig. 9 represent the actual minimum values of $R = 3.34$ and $A = 14.51$ that can support patterning. They were extracted numerically using `pde2path` by calculating the stable/unstable transition bifurcation point on the subcritical bifurcation branch.

So far we have compared only the linear stability analysis and the first bifurcation point. We now extend this to compare the weakly nonlinear analysis with the computed bifurcation structure. For the Schnakenberg kinetics on the triangular domain, we find that the nontrivial steady-state amplitudes of equations (68) and (69) are

$$\left(\frac{9S_1\sqrt{2}}{40\pi}, 0\right), \quad \left(\frac{-9S_1\sqrt{2}}{80\pi}, \pm\frac{9\sqrt{6}S_1}{80\pi}\right). \tag{74}$$

The first term represents a heterogeneous solution made up of only the symmetric solution, whilst the second and third solutions are mixed superposition solutions. Critically, as we will see, we only ever observe the symmetric solutions bifurcating from R_c. The only time the superposition solutions are seen are as a branch of unstable solutions that switch between symmetric solutions that have the point highest and those that have the point lowest. Thus, for now it is still an unanswered question as to why we never observe superposition solutions bifurcating from R_c. Namely, are the solutions

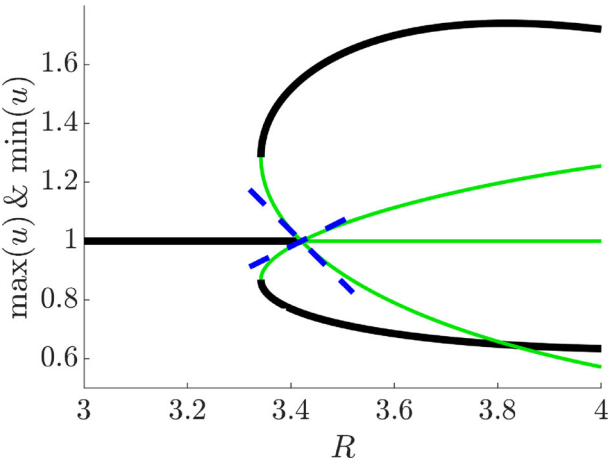

Fig. 10 Bifurcation diagram of equations (71) and (72) (black and green) compared with the solution derived through weakly nonlinear analysis equations (75) and (76) (blue lines). The black lines represent the maxima and minima of stable solutions, whereas the green lines represent the maxima and minima of unstable solutions (Color figure online)

there and the numerical simulations not picking them up? Or is there some other constraint that we are not seeing in the weakly nonlinear analysis at the second order expansion that means that the superposition solutions never bifurcate from R_c?

Going forward we focus purely on the symmetric solutions only. The maximum and minimum of h_{s10} are 3 and -3/2, respectively. Thus, we compare the numerically derived bifurcation structure, which tracks the maximum and minimum of the solution u with

$$u_+ = u_s + 3\epsilon S_1 \Lambda \frac{p_2}{p_1} = 1 + \epsilon S_1 \frac{9\sqrt{2}}{4\pi} = 1 + \epsilon R_1 \frac{9\sqrt{6}}{4\pi} = 1 + (R - R_c)\frac{9\sqrt{6}}{4\pi}, \quad (75)$$

$$u_- = u_s - \frac{3}{2}\epsilon S_1 \Lambda \frac{p_2}{p_1} = 1 - \epsilon S_1 \frac{9\sqrt{2}}{8\pi} = 1 - \epsilon R_1 \frac{9\sqrt{6}}{8\pi} = 1 - (R - R_c)\frac{9\sqrt{6}}{8\pi}. \quad (76)$$

where $\Lambda = -10/3$ was calculated using Table 2 and equation (57). Note that u_+ and u_- swap their roles of maximum and minimum as R_1 (or S_1) transitions from negative to positive. Figure 10 illustrates the numerically derived bifurcation diagram (black and green lines), compared with equations (75) and (76). Of course, the blue lines being the tangents of the bifurcation structure cannot capture its nonlinear complexity. However, near R_c the blue lines well match the bifurcation lines. Further, as predicted in Sect. 6.2, all patterns bifurcate in an unstable manner from R_c. The stable patterns that appear once the homogeneous steady states have destabilised stem from the subcritical branch stabilising at approximately $R = 3.34$ (see Fig. 9).

The results for the square domain are similar. Amplitude equations (63) and (64) have the exact values

$$\frac{\mathrm{d}a}{\mathrm{d}t_2} = -\frac{125}{27}a^3 + \frac{135\sqrt{2}S_2 - 750b^2}{513\pi}a, \tag{77}$$

$$\frac{\mathrm{d}b}{\mathrm{d}t_2} = -\frac{125}{27}b^3 + \frac{135\sqrt{2}S_2 - 750a^2}{513\pi}b. \tag{78}$$

The steady states are:

1. $(0, 0)$, which is stable for $S < S_c$ and unstable for $S > S_c$;
2. $\left(\frac{3\sqrt{3}\sqrt{19}}{95}\sqrt{\frac{S_2\sqrt{2}}{\pi}}, 0\right)$, which only exists for $S > S_c$ and is unstable;
3. $\left(\frac{3\sqrt{3}}{25}\sqrt{\frac{S_2\sqrt{2}}{\pi}}, \frac{3\sqrt{3}}{25}\sqrt{\frac{S_2\sqrt{2}}{\pi}}\right)$, which only exists for $S > S_c$ and is stable.

The maximum and the minimum of the stripe basis solutions are ± 1, respectively, whereas the maximum and minimum of the spot basis solutions are ± 2, respectively, since we are adding two solutions together. Thus, the maximum and minimum of the stripe solutions are

$$u_+ = u_s + \epsilon\Lambda\frac{3\sqrt{3}\sqrt{19}}{95}\sqrt{\frac{S_2\sqrt{2}}{\pi}} = 1 + \frac{10\sqrt{6}\sqrt{19}}{95}\sqrt{\frac{R - R_c}{\pi}}, \tag{79}$$

$$u_- = u_s - \epsilon\Lambda\frac{3\sqrt{3}\sqrt{19}}{95}\sqrt{\frac{S_2\sqrt{2}}{\pi}} = 1 + \frac{10\sqrt{6}\sqrt{19}}{95}\sqrt{\frac{R - R_c}{\pi}}, \tag{80}$$

and the maximum and minimum of the spot solutions are

$$u_+ = u_s + 2\epsilon\Lambda\frac{3\sqrt{3}}{25}\sqrt{\frac{S_2\sqrt{2}}{\pi}} = 1 + \frac{20\sqrt{6}}{25}\sqrt{\frac{R - R_c}{\pi}}, \tag{81}$$

$$u_- = u_s - 2\epsilon\Lambda\frac{3\sqrt{3}}{25}\sqrt{\frac{S_2\sqrt{2}}{\pi}} = 1 + \frac{20\sqrt{6}}{25}\sqrt{\frac{R - R_c}{\pi}}. \tag{82}$$

From Fig. 11 and the analysis from Sect. 6.1, we see that the weakly nonlinear analysis accurately represents the bifurcation structure near R_c in both shape and stability. Namely, although both bifurcation branches have a pitchfork shape, only one of the spot and stripe patterns bifurcates stable into $R > R_c$; in this case, it is the spot solution that is stable.

7.3 Beyond weakly nonlinear analysis

Having considered the bifurcation structure near R_c, we now use `pde2path` to expand our knowledge of the bifurcation structure for all polygons with less than 10 edges, with the aim of generalising our understanding as the number of edges increases.

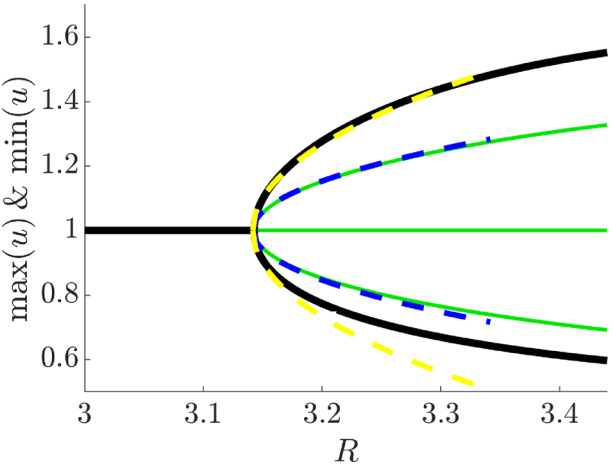

Fig. 11 Bifurcation diagram of equations (71) and (72) (black and green) compared with the solution derived through weakly nonlinear analysis equations (79)–(82) (dashed lines). The black lines represent the maxima and minima of stable solutions, whereas the green lines represent the maxima and minima of unstable solutions. The blue dashed lines represent equations (79) and (80) and show that these solutions are unstable, whilst the yellow dashed lines represent equations (81) and (82) and show that the solutions are stable (Color figure online)

Figure 12 illustrates the bifurcation diagrams for equilateral triangles, squares and pentagons, as well as providing simulations along each of stable and unstable branches. Note that in all bifurcation diagrams we focus on the appearance and subsequent disappearance of the first branches bifurcating from R_c. If R increases further, the bifurcation diagram continues to grow in complexity as more and more wave modes are able to destabilise at the same time.

Going forward we introduce a new piece of nomenclature, which we will use to describe visual appearance of the patterns during the first bifurcation. We will use the terms edge-up or corner-up patterns to specify when the highest value of the simulation is seen along an edge or in a corner, respectively. As specific examples, consider the top row of Fig. 12b. The top left subfigure is a corner-up pattern, whereas the top right subfigure is an edge-up pattern. This may appear to be a crude description, but we will see that is can be used to accurately describe most patterns, at least when the number of edges $n < 8$. However, as we increase the number of edges, the edges decrease in size and the corners become more numerous, so specifying whether a pattern is edge-up or corner-up becomes more difficult, visually.

In the case of the equilateral triangular bifurcation diagram (top of Fig. 12a), we reproduce the insights from Sect. 7.2; namely, only the symmetric solutions bifurcate from R_c and the branches bifurcate in an unstable manner through a transcritical structure. However, we see that at around $R = 4.5$ the stable branch flips. Using Fig. 12b, we can see that the stability transition occurs between corner-up patterns and edge-up patterns (compare the top and bottom subfigure of Fig. 12b.

Note that there is a small but nontrivial region around $R \approx 4.5$ in which both orientations are stable and there is an unstable branch of solutions linking the two

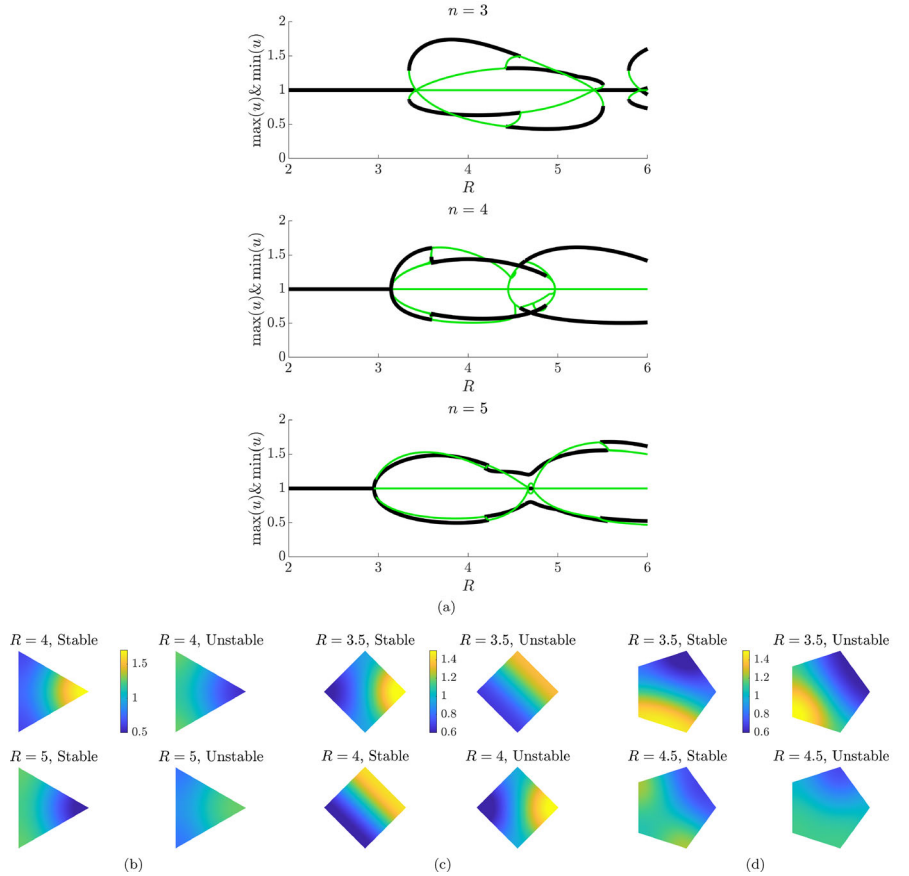

Fig. 12 **a** Bifurcation diagrams for equilateral triangles, squares and pentagons, top to bottom, respectively. The n in the title of each subfigure represents the number of edges each regular polygon has. The black lines represent the maxima and minima of stable solutions. The green lines represent the maxima and minima of unstable solutions. **b–d** Patterns simulated on the equilateral triangle, square and pentagon domains, respectively. The simulations present solutions on the stable and unstable branches at the given values of R in the subfigure titles. The colour bar is given in the centre of the top row of four simulations (Color figure online)

stable branches. This unstable linking is a set of antisymmetric solutions which allow the solutions to transition between these the edge-up and corner-up orientations. Thus, not only are antisymmetric solutions prohibited from bifurcating at R_c, we observe that even when they occur their branch is unstable. Thus, the first set of unstable patterns (whether edge-up or corner-up) are all symmetric, the only choice stems from which orientation is stable.

A similar structure can be seen over all three bifurcation diagrams in Fig. 12a. Namely during the first bifurcation there are two branches that appear: one has stable solutions, and one has unstable solutions. Moreover, there is always a small branch joining the two initial branches, which causes the stability of the branches to switch.

This is perhaps most clearly shown in Fig. 12b-d, where in the top row of each figure we fix a value of R and present the stable and unstable patterns that are present. For the equilateral triangle, corner-up patterns are stable and the edge-up patterns are unstable. This is similar to the square domain where we corner-up patterns are stable, whilst edge-up patterns are unstable. The stability orientation then appears to flip for the pentagon, where we see that the edge-up patterns are stable, whilst corner-up patterns are unstable.

If we now consider the bottom row of Fig. 12b–d and compare them to the top row, we observe the stability transition in Fig. 12a that occurs as R increases. For example, in Fig. 12b-d, the corner-up pattern that was stable at $R = 4$ is now unstable at $R = 5$. Vice versa, the edge-up pattern that was unstable at $R = 4$ is not stable at $R = 5$. This stability swapping clearly occurs also in Fig. 12c–d.

Although there are similarities in behaviour, we do observe that the bifurcation diagrams illustrated in Fig. 12a are fairly different. Firstly, as proven, the equilateral triangles bifurcation structure is fundamentally different from the other two structures because it presents a transcritical bifurcation and, thus, has subcritical stable patterns possible, whereas the bifurcations of the square and pentagon are both supercritical. Equally, we can observe that, as demonstrated in Fig. 9a, the minimum point at which the homogeneous steady-state destabilises, R_c, decreases with increasing number of edges. Further, there does not appear to be any consistency between the point of stable pattern transition, as we observe that the stability transition on the square happens around $R = 3.5$, whereas the transition happens later (*i.e.* $R > 4$) on the equilateral triangle and pentagon.

Finally, as the number of edges increases, the higher-order patterning modes begin to encroach and become entangled with the first bifurcation modes. Namely, for the triangle the is a region around $R = 5.6$ where patterns would actually disappear as the homogeneous steady state stabilises and the initial bifurcation branches has disappeared; thus, no patterned states exist. However, for the square we see that the stability of the first bifurcation branches smoothly transition into higher-order branches, so that only patterned states exist. Finally, on the pentagon, we get a mixture of these two features. Firstly, the first bifurcation modes transition smoothly into the higher-order pattern curves, whilst at the same time, around $R = 4.7$, there is a small region in which the homogeneous steady state stabilises alongside the patterned states.

Based on the insights gained from Fig. 12, we might wonder how far observations can be generalised between bifurcation diagrams of regular polygon domain. However, once the number of edges is 6, or more, the bifurcation diagrams appear to be fairly comparative (see Fig. 13a). Note simulations were also run for polygons with edges $n = 7, 9, 100, 101$ and 150. However, these bifurcation figures have been omitted as they do not vary from those illustrated in Fig. 13a. In Fig. 13b–f, we present pattern simulations on all regular polygons with edges $n = 6 - 10$ as a means of considering whether the edge-up to corner-up stability transition changes as n becomes larger.

Firstly, we compare the bifurcation structures across Fig. 13a with those in Fig. 12a and we immediately observe that whereas the bifurcation diagrams had more differences than similarities for polygons with edges $n = 2 - 5$, the bifurcation structures for polygons with edges $n \geq 6$ are all pretty similar. As before there are

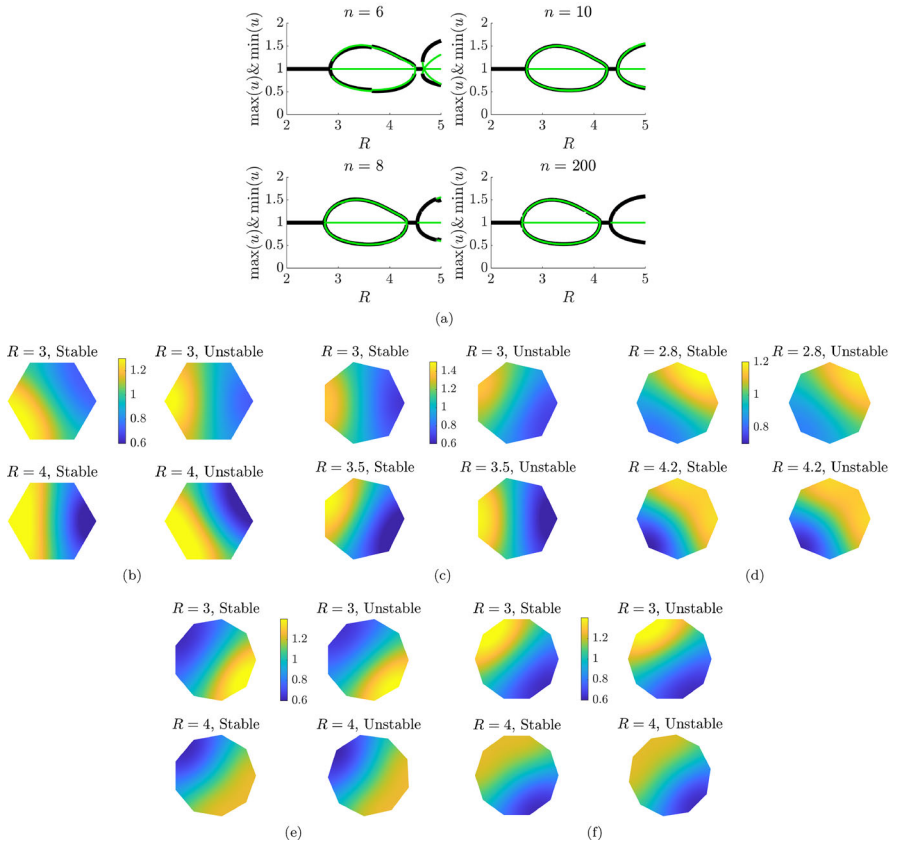

Fig. 13 **a** Bifurcation diagrams for equilateral triangles, squares and pentagons, top to bottom, respectively. The n in the title of each subfigure represents the number of edges each regular polygon has. The black lines represent the maxima and minima of stable solutions. The green lines represent the maxima and minima of unstable solutions. **b–f** Patterns simulated on polygons of increasing number of edges, respectively. The simulations present solutions on the stable and unstable branches at the given values of R in the subfigure titles. The colour bar is given in the centre of the top row of four simulations (Color figure online)

two branches of solutions initially. One is stable, and one is unstable; critically, these two branches practically lie over one another in Fig. 13a.

Specifically, we note that although the stability transition is still visible in the hexagon bifurcation plot of Fig. 13a, by the time we get to $n = 8$ and higher the bifurcation branches are so close that we can no longer see the transition in the bifurcation diagrams and must instead use the simulations in Fig. 13d–f.

For domains with relatively low number of edges, $n = 6$ and 7, say, there two initial branches appear to present patterns that can be described as edge-up or corner-up and that the transition between these two pattern orientations still exist. For example, the top row of Fig. 13b, c demonstrates that edge-up patterns are stable, whilst the corner-up patterns are unstable, for $R = 3$; however, the bottom rows Fig. 13b, c show that as R increases, the corner-up patterns stabilise, whilst the edge-up patterns destabilise.

For domains with larger numbers of edges, it becomes increasingly more difficult to specify what an edge-up vs what a corner-up pattern is, because edges become smaller and more corners are added. Indeed, as suggested in Fig. 13a not only do the bifurcation diagrams converge, but the difference between an unstable and a stable pattern becomes negligible. Namely, on a polygonal domain with large enough number of edges there is a stable pattern that is practically indiscernible from a given unstable pattern.

Another common feature across all bifurcation diagrams with $n \geq 6$ is that the bifurcation structure of the first mode is isolated from the destabilisation of the higher order modes, which is more like the $n = 3$ case of Fig. 12a, rather than the $n = 4$ and $n = 5$ cases, which we might expect would be more similar to the $n \geq 6$ cases since they are closer in terms of number of edges.

Overall, as the number of edges increases the polygons tend to the shape of a circle, we would expect an eventual convergence of the bifurcation structures. Of course we can never present a bifurcation structure for an exact circle because simulations, by their very nature, are discrete and, thus, the circle would have to be approximated to a polygon with large number of edges. Thus, the convergence in bifurcation diagrams for $n \geq 8$ offers confidence in the fact that a simulation does not have to be too refined, before it accurately represents the bifurcation structure of circle.

We should be mindful of the limitations of simulations. Namely, although the simulations appear to converge, there will be some differences between these bifurcation diagrams and one of a true circle. Specifically, as shown in Fig. 9 the bifurcation point heavily depends on the number of edges, and thus, we suggest that you need $n \geq 20$ before you are within an acceptable tolerance of bifurcation point calculation.

Further, for any discrete simulation two branches initially appear at R_c, one stable and one unstable representing the edge-up and corner-up solutions. However, as the number of edges increases, it becomes increasingly more difficult to discern whether a pattern in edge-up or corner-up, see Fig. 13f, in particular. Thus, we hypothesise that in the limit of $n \to \infty$ and the polygons tending to a true circle the unstable branch will actually disappear because we know that stable patterns exist and there would no longer be a difference between edge-up and corner-up patterns.

8 Conclusions

We have investigated how regular polygonal domains with zero-flux boundary conditions influence the initial patterning instability of Turing unstable reaction–diffusion systems. The reason for this is that many theory and application papers frequently only use simple domains such as squares and rectangles. The reason for this is easy to understand; the Turing instability is analytically tractable (at least to a weakly nonlinear level) on such domains. However, as Sect. 7 has shown, changing the domain shape can lead to fundamental changes in the generic structure of the bifurcation diagram (see Fig. 12a).

Further, we have highlighted the nonlinear relationship between number of polygonal edges and the bifurcation point (see Fig. 9). Of course we should not be surprised that the circle bifurcates first, as the circumcentre radius grows. The circle has the

largest area for a given perimeter, and we know that the Turing bifurcation only occurs if the domain's size is large enough. However, what was perhaps unexpected was that even though a larger circumcentre is required before the equilateral triangle bifurcates, the bifurcation area of the triangle is smaller than that of the circle. Critically, the area reduction is a nontrivial 32% in the case of the Schnakenberg kinetics.

Note that we specify that the relationships between bifurcation point, edges and area are nonlinear, but we have been unable to identify the relationship beyond this. Specifically, the relationships do not appear to be power laws as using logarithmic scales for the axes fails to return linear relationships. Thus, we leave this relationship as an open question for the community.

Such relationships and dependencies between size and bifurcation values highlight the requirement of using a suitable domain shape in applications (Woolley et al. 2010). Namely, we should be sceptical of any work that uses square geometries and claims that bifurcations cannot occur because the space is too small, because, as we have shown, the bifurcation point can easily be reduced by increasing the number of edges.

Luckily, with modern numerical software, it is not too difficult to create more accurate, complex geometries that go beyond the simple symmetries of the regular polygons. However, this work is still useful in its ability to theoretically highlight the need for such accurate domain generation.

Overall, this article can be considered as a partner to (Woolley 2022), which demonstrates that minimal changes to the boundary conditions can also fundamentally change the bifurcation structure, which is not observed in the linear kinetics. Thus, if minor changes in the boundary conditions and/or shape can lead to extreme changes in patterning behaviour, application papers must be heavily critical about the solution domains and we suggest that spatial perturbations in shape and boundary conditions should become normalised as part of patterning investigations.

Appendix A: Expansion solutions

A.1 Solving the second order expansion on a square domain

If we assume that there is no t_1 dependence and that $S_1 = 0$, then upon substitution of $\boldsymbol{U}_1$ the right-hand side of equation (53) is explicitly

$$\mathcal{L}\boldsymbol{U}_2 = -\frac{a^2}{4}\begin{pmatrix}\Lambda^2 f_{uu} + 2\Lambda f_{uv} + f_{vv}\\ \Lambda^2 g_{uu} + 2\Lambda g_{uv} + g_{vv}\end{pmatrix} \left(\cos(2\pi x) + 4C_s\cos(\pi x)\cos(\pi y) + C_s\cos(2\pi y) + (C_s^2+1)\right). \tag{A1}$$

By inspection, $\boldsymbol{U}_2$ must have the form,

$$\boldsymbol{U}_2 = \begin{pmatrix}U_{2c}\\ V_{2c}\end{pmatrix} + \begin{pmatrix}U_{2x}\\ V_{2x}\end{pmatrix}\cos(2\pi x) + \begin{pmatrix}U_{2xy}\\ V_{2xy}\end{pmatrix}\cos(\pi x)\cos(\pi y) + \begin{pmatrix}U_{2y}\\ V_{2y}\end{pmatrix}\cos(2\pi y) + \alpha\boldsymbol{U}_1, \tag{A2}$$

where α is an arbitrary constant that could be used to fit the initial conditions. Here, for simplicity we set it to 0. After substituting equation (A2) into equation (A1), we can solve for the eight undetermined coefficients of equation (A2),

$$U_{2c} = -\frac{\left(\left(-\Lambda^2 g_{uu} - 2\Lambda g_{uv} - g_{vv}\right) f_v + g_v\left(\Lambda^2 f_{uu} + 2\Lambda f_{uv} + f_{vv}\right)\right)\left(a^2+b^2\right)}{4 f_u g_v - 4 f_v g_u}, \tag{A3}$$

$$U_{2x} = \frac{\left(\left(\left(f_{uu} g_v - f_v g_{uu}\right)\Lambda^2 + \left(2 f_{uv} g_v - 2 f_v g_{uv}\right)\Lambda + g_v f_{vv} - f_v g_{vv}\right) {S_c}^2 - 4\pi^2 D_v\left(\Lambda^2 f_{uu} + 2\Lambda f_{uv} + f_{vv}\right)\right) a^2 {S_c}^2}{\left(-4 f_u g_v + 4 f_v g_u\right) {S_c}^4 + 16\pi^2\left(D_u g_v + D_v f_u\right) {S_c}^2 - 64 D_u D_v \pi^4}, \tag{A4}$$

$$U_{2y} = \frac{\left(\left(\left(f_{uu} g_v - f_v g_{uu}\right)\Lambda^2 + \left(2 f_{uv} g_v - 2 f_v g_{uv}\right)\Lambda + g_v f_{vv} - f_v g_{vv}\right) {S_c}^2 - 4\pi^2 D_v\left(\Lambda^2 f_{uu} + 2\Lambda f_{uv} + f_{vv}\right)\right) b^2 {S_c}^2}{\left(-4 f_u g_v + 4 f_v g_u\right) {S_c}^4 + 16\pi^2\left(D_u g_v + D_v f_u\right) {S_c}^2 - 64 D_u D_v \pi^4}, \tag{A5}$$

$$U_{2xy} = \frac{{S_c}^2 b\left(\left(\left(f_{uu} g_v - f_v g_{uu}\right)\Lambda^2 + \left(2 f_{uv} g_v - 2 f_v g_{uv}\right)\Lambda + g_v f_{vv} - f_v g_{vv}\right) {S_c}^2 - 2\pi^2 D_v\left(\Lambda^2 f_{uu} + 2\Lambda f_{uv} + f_{vv}\right)\right) a}{\left(-f_u g_v + f_v g_u\right) {S_c}^4 + 2\pi^2\left(D_u g_v + D_v f_u\right) {S_c}^2 - 4 D_u D_v \pi^4}, \tag{A6}$$

$$V_{2c} = \frac{\left(a^2+b^2\right)\left(\left(-\Lambda^2 g_{uu} - 2\Lambda g_{uv} - g_{vv}\right) f_u + g_u\left(\Lambda^2 f_{uu} + 2\Lambda f_{uv} + f_{vv}\right)\right)}{4 f_u g_v - 4 f_v g_u}, \tag{A7}$$

$$V_{2x} = -\frac{\left(\left(\left(-f_u g_{uu} + g_u f_{uu}\right)\Lambda^2 + \left(-2 f_u g_{uv} + 2 g_u f_{uv}\right)\Lambda + g_u f_{vv} - f_u g_{vv}\right) {S_c}^2 + 4\pi^2 D_u\left(\Lambda^2 g_{uu} + 2\Lambda g_{uv} + g_{vv}\right)\right) a^2 {S_c}^2}{\left(-4 f_u g_v + 4 f_v g_u\right) {S_c}^4 + 16\pi^2\left(D_u g_v + D_v f_u\right) {S_c}^2 - 64 D_u D_v \pi^4}, \tag{A8}$$

$$V_{2y} = -\frac{\left(\left(\left(-f_u g_{uu} + g_u f_{uu}\right)\Lambda^2 + \left(-2 f_u g_{uv} + 2 g_u f_{uv}\right)\Lambda + g_u f_{vv} - f_u g_{vv}\right) {S_c}^2 + 4\pi^2 D_u\left(\Lambda^2 g_{uu} + 2\Lambda g_{uv} + g_{vv}\right)\right) b^2 {S_c}^2}{\left(-4 f_u g_v + 4 f_v g_u\right) {S_c}^4 + 16\pi^2\left(D_u g_v + D_v f_u\right) {S_c}^2 - 64 D_u D_v \pi^4}, \tag{A9}$$

$$V_{2xy} = -\frac{{S_c}^2 b\left(\left(\left(-f_u g_{uu} + g_u f_{uu}\right)\Lambda^2 + \left(-2 f_u g_{uv} + 2 g_u f_{uv}\right)\Lambda + g_u f_{vv} - f_u g_{vv}\right) {S_c}^2 + 2\pi^2 D_u\left(\Lambda^2 g_{uu} + 2\Lambda g_{uv} + g_{vv}\right)\right) a}{\left(-f_u g_v + f_v g_u\right) {S_c}^4 + 2\pi^2\left(D_u g_v + D_v f_u\right) {S_c}^2 - 4 D_u D_v \pi^4} \tag{A10}$$

These coefficients are then used in the calculation of the solvability criterion, see equations (A12) and (A13).

A.2 Solvability criterion

Applying Fredholm's alternative theorem to equation (54) means that we have to satisfy

$$\langle \boldsymbol{W}, \mathcal{L}\boldsymbol{U}_3 \rangle = 0. \tag{A11}$$

for each of the basis function $\boldsymbol{W}$, given in equation (59). Inserting equations (56) and (A2) into the right-hand side of equation (54) and taking the inner product with equation (59) mean that we have to satisfy

$$\begin{aligned} 0 =& (\Gamma\Lambda + 1)\frac{\mathrm{d}a}{\mathrm{d}t_2} + \left(-\frac{1}{8}\left(f_{uuu}\Gamma + g_{uuu}\right)\Lambda^3 - \frac{3}{8}\left(f_{uuv}\Gamma + g_{uuv}\right)\Lambda^2 \right. \\ & \left. -\frac{3}{8}\left(f_{uvv}\Gamma + g_{uvv}\right)\Lambda - \frac{1}{8}\left(\Gamma f_{vvv} + g_{vvv}\right)\right) a^3 \\ & + \left(\left(-\frac{1}{4}\left(f_{uuu}\Gamma + g_{uuu}\right)\Lambda^3 + -\frac{3}{4}\left(f_{uuv}\Gamma + g_{uuv}\right)\Lambda^2 \right.\right. \end{aligned}$$

$$
\begin{aligned}
&-\frac{3}{4}\left(f_{uvv}\Gamma+g_{uvv}\right)\Lambda-\frac{1}{4}\left(\Gamma f_{vvv}+g_{vvv}\right)\Big)b^2\\
&+\Bigg(\frac{1}{2}\Bigg(-\left(2U_{2c}+U_{2x}\right)f_{uu}-\left(2V_{2c}+V_{2x}\right)f_{uv}-4\frac{S_2\pi^2D_u}{{S_c}^3}\Bigg)\Gamma\\
&-\frac{1}{2}\left(2U_{2c}+U_{2x}\right)g_{uu}-\frac{1}{2}g_{uv}\left(2V_{2c}+V_{2x}\right)\Bigg)\Lambda\\
&+\Bigg(-\frac{1}{2}\left(2U_{2c}+U_{2x}\right)f_{uv}-\frac{1}{2}\left(2V_{2c}+V_{2x}\right)f_{vv}\Bigg)\Gamma\\
&+\frac{1}{2}\Bigg(-\left(2U_{2c}+U_{2x}\right)g_{uv}-\left(2V_{2c}+V_{2x}\right)g_{vv}-4\frac{S_2\pi^2D_v}{{S_c}^3}\Bigg)\Bigg)a\\
&-\frac{1}{2}\Big(\Big(\left(f_{uv}V_{2xy}+f_{uu}U_{2xy}\right)\Gamma+g_{uu}U_{2xy}+g_{uv}V_{2xy}\Big)\Lambda\\
&+\left(f_{vv}V_{2xy}+f_{uv}U_{2xy}\right)\Gamma+g_{vv}V_{2xy}+g_{uv}U_{2xy}\Big)b,
\end{aligned}
\tag{A12}
$$

$$
\begin{aligned}
0=&\left(\Gamma\Lambda+1\right)\frac{\mathrm{d}b}{\mathrm{d}t_2}+\Bigg(-\frac{1}{8}\left(f_{uuu}\Gamma+g_{uuu}\right)\Lambda^3-\frac{3}{8}\left(f_{uuv}\Gamma+g_{uuv}\right)\Lambda^2\\
&-\frac{3}{8}\left(f_{uvv}\Gamma+g_{uvv}\right)\Lambda-\frac{1}{8}\left(\Gamma f_{vvv}+g_{vvv}\right)\Bigg)b^3\\
&+\Bigg(\Bigg(-\frac{1}{4}\left(f_{uuu}\Gamma+g_{uuu}\right)\Lambda^3+-\frac{3}{4}\left(f_{uuv}\Gamma+g_{uuv}\right)\Lambda^2\\
&-\frac{3}{4}\left(f_{uvv}\Gamma+g_{uvv}\right)\Lambda-\frac{1}{4}\left(\Gamma f_{vvv}+g_{vvv}\right)\Bigg)a^2\\
&+\Bigg(\frac{1}{2}\Bigg(-\left(2U_{2c}+U_{2y}\right)f_{uu}-\left(2V_{2c}+V_{2y}\right)f_{uv}-4\frac{S_2\pi^2D_u}{{S_c}^3}\Bigg)\Gamma\\
&-\frac{1}{2}\left(2U_{2c}+U_{2y}\right)g_{uu}-\frac{1}{2}g_{uv}\left(2V_{2c}+V_{2y}\right)\Bigg)\Lambda\\
&+\Bigg(-\frac{1}{2}\left(2U_{2c}+U_{2y}\right)f_{uv}-\frac{1}{2}\left(2V_{2c}+V_{2y}\right)f_{vv}\Bigg)\Gamma\\
&+\frac{1}{2}\Bigg(-\left(2U_{2c}+U_{2y}\right)g_{uv}-\left(2V_{2c}+V_{2y}\right)g_{vv}-4\frac{S_2\pi^2D_v}{{S_c}^3}\Bigg)\Bigg)b\\
&-\frac{1}{2}\Big(\Big(\left(f_{uv}V_{2xy}+f_{uu}U_{2xy}\right)\Gamma+g_{uu}U_{2xy}+g_{uv}V_{2xy}\Big)\Lambda\\
&+\left(f_{vv}V_{2xy}+f_{uv}U_{2xy}\right)\Gamma+g_{vv}V_{2xy}+g_{uv}U_{2xy}\Big)a
\end{aligned}
\tag{A13}
$$

From Sect. A1, we note that each of the U_i and V_i contains a term of the form a^2, b^2, both or ab. Substituting these terms into equations (A12) and (A13), we arrive at an equations of the form given by equations (63) and (64).

Author Contributions T.E.W. conceived and designed the study, developed and executed the mathematical analysis and simulations, prepared all figures and wrote the main manuscript text.

Data availability No datasets were generated or analysed during the current study.

Declarations

Conflict of interest The authors declare no conflict of interest.

References

Adamer, M.F., Harrington, H.A., Gaffney, E.A., Woolley, T.E.: Coloured noise from stochastic inflows in reaction-diffusion systems. Bull. Math. Biol. **82**(4), 44 (2020)

Aragón, J.L., Barrio, R.A., Woolley, T.E., Baker, R.E., Maini, P.K.: Nonlinear effects on turing patterns: time oscillations and chaos. Phys. Rev. E **86**(2), 026201 (2012)

Auchmuty, J.F.G., Nicolis, G.: Bifurcation analysis of nonlinear reaction-diffusion equations-I. Evolution equations and the steady state solutions. B. Math. Biol. **37**(4), 323–365 (1975)

Baricz, Á., Kokologiannaki, C., Pogány, T.: Zeros of Bessel function derivatives. Proc. Am. Math. Soc. **146**(1), 209–222 (2018)

Barrass, I., Crampin, E.J., Maini, P.K.: Mode transitions in a model reaction-diffusion system driven by domain growth and noise. Bull. Math. Biol. **68**(5), 981–995 (2006)

Becherer, P., Morozov, A.N., van Saarloos, W.: Probing a subcritical instability with an amplitude expansion: an exploration of how far one can get. Physica D **238**(18), 1827–1840 (2009)

Benson, D.L., Maini, P.K., Sherratt, J.A.: Unravelling the Turing bifurcation using spatially varying diffusion coefficients. J. Math. Biol. **37**(5), 381–417 (1998)

Bozzini, B., Gambino, G., Lacitignola, D., Lupo, S., Sammartino, M., Sgura, I.: Weakly nonlinear analysis of Turing patterns in a morphochemical model for metal growth. Comput. Math. Appl. **70**(8), 1948–1969 (2015)

Breña-Medina, V., Champneys, A.: Subcritical Turing bifurcation and the morphogenesis of localized patterns. Phys. Rev. E **90**(3), 032923 (2014)

Cho, S.W., Kwak, S., Woolley, T.E., Lee, M.J., Kim, E.J., Baker, R.E., Kim, H.J., Shin, J.S., Tickle, C., Maini, P.K., Jung, H.S.: Interactions between Shh, Sostdc1 and Wnt signaling and a new feedback loop for spatial patterning of the teeth. Development **138**, 1807–1816 (2011)

COMSOL Multiphysics. v. 5.1. www.comsol.com (2021)

Crampin, E.J.: Reaction-Diffusion Patterns on Growing Domains. PhD thesis, University of Oxford (2000)

Crampin, E.J., Gaffney, E.A., Maini, P.K.: Reaction and diffusion on growing domains: scenarios for robust pattern formation. Bull. Math. Biol. **61**(6), 1093–1120 (1999)

Dalwadi, M.P., Pearce, P.: Universal dynamics of biological pattern formation in spatio-temporal morphogen variations. bioRxiv (2022)

Damle, A., Peterson, G.C.: Understanding the eigenstructure of various triangles. SIAM Undergrad. Res. Online **3**(1), 187–208 (2010)

De Kepper, P., Castets, V., Dulos, E., Boissonade, J.: Turing-type chemical patterns in the chlorite-iodide-malonic acid reaction. Physica D **49**(1–2), 161–169 (1991)

Diego, X., Marcon, L., Müller, P., Sharpe, J.: Key features of Turing systems are determined purely by network topology. Phys. Rev. X **8**(2), 021071 (2018)

Dillon, R., Maini, P.K., Othmer, H.G.: Pattern formation in generalized Turing systems. J. Math. Biol. **32**(4), 345–393 (1994)

Dohnal, T., Rademacher, J.D.M., Uecker, H., Wetzel, D.: pde2path 2.0: multi-parameter continuation and periodic domains. In: H. Ecker, A. Steindl, and S. Jakubek, editors, Proceedings of 8th European Nonlinear Dynamics Conference (2014)

Dutt, A.K.: Turing pattern amplitude equation for a model glycolytic reaction-diffusion system. J. Math. Chem., pp. 1–15 (2010)
Dutt, A.K.: Amplitude equation for a diffusion-reaction system: the reversible Sel'kov model. AIP Adv. **2**(4), 042125 (2012)
Economou, A.D., Ohazama, A., Porntaveetus, T., Sharpe, P. T., Kondo, S., Basson, M.A., Gritli-Linde, A., Cobourne, M.T., Green, J.B.A.: Periodic stripe formation by a Turing mechanism operating at growth zones in the mammalian palate. Nat. Genet., pp. 1546–1718 (2012)
Elbert, Á.: An approximation for the zeros of Bessel functions. Numer. Math. **59**(1), 647–657 (1991)
Engelnkemper, S., Gurevich, S. V., Uecker, H., Wetzel, D., Thiele, U.: Continuation for thin film hydrodynamics and related scalar problems. In: Computational modelling of bifurcations and instabilities in fluid dynamics. Springer, pp. 459–501 (2019)
Fokas, A.S., Kalimeris, K.: Eigenvalues for the Laplace operator in the interior of an equilateral triangle. Comput. Methods Funct. Theory **14**(1), 1–33 (2014)
Fuseya, Y., Katsuno, H., Behnia, K., Kapitulnik, A.: Nanoscale Turing patterns in a bismuth monolayer. Nat. Phys. **17**(9), 1031–1036 (2021)
Gierer, A., Meinhardt, H.: A theory of biological pattern formation. Biol. Cybern. **12**(1), 30–39 (1972)
Giordano, C., Laforgia, A.: Elementary approximations for zeros of Bessel functions. J. Comput. Appl. Math. **9**(3), 221–228 (1983)
Grebenkov, D.S., Nguyen, B.-T.: Geometrical structure of Laplacian eigenfunctions. SIAM Rev. **55**(4), 601–667 (2013)
Grindrod, P.: The Theory and Applications of Reaction-Diffusion Equations: Patterns and Waves. Clarendon Press (1996)
Gutiérrez-Vega, J.C., Rodrıguez-Dagnino, R.M., Meneses-Nava, M.A., Chávez-Cerda, S.: Mathieu functions, a visual approach. Am. J. Phys. **71**(3), 233–242 (2003)
Hans, I., Harn, C., Wang, S.-P., Lai, Y.-C., Van Handel, B., Liang, Y.-C., Tsai, S., Schiessl, I.M., Sarkar, A., Xi, H., Hughes, M., Kaemmer, S., Tang, M.J., Peti-Peterdi, J., Pyle, A.D., Woolley, T.E., Evseenko, D., Jiang, T.-X., Chuong, C.-M.: Symmetry breaking of tissue mechanics in wound induced hair follicle regeneration of laboratory and spiny mice. Nature Commun. **12**(1), 1–16 (2021)
Hardy, G.H., Wright, E.M.: An Introduction to the Theory of Numbers. Oxford University Press, Oxford (1979)
Harrison, J.: Fast and accurate Bessel function computation. In: 2009 19th IEEE Symposium on Computer Arithmetic, pp. 104–113 (2009)
Ho, W.K.W., Freem, L., Zhao, D., Painter, K.J., Woolley, T.E., Gaffney, E.A., McGrew, M.J., Tzika, A., Milinkovitch, M.C., Schneider, P., Drusko, A., Matthäus, F., Glover, J.D., Wells, K.L., Johansson, J.A., Davey, M.G., Sang, H.M., Clinton, M., Headon, D.J.: Feather arrays are patterned by interacting signalling and cell density waves. PLoS Biol. **17**(2), 1–38 (2019)
Jones, D.S.: Acoustic and Electromagnetic Waves. Oxford/New York (1986)
Khosravian-Arab, H., Dehghan, M., Eslahchi, M.R.: Generalized Bessel functions: theory and their applications. Math. Methods Appl. Sci. **40**(18), 6389–6410 (2017)
Kondo, S., Asai, R.: Turing patterns in fish skin? Nature **380**(6576), 678–678 (1996)
Krause, A. L., Klika, V., Woolley, T. E., Gaffney, E. A.: Heterogeneity induces spatiotemporal oscillations in reaction-diffusion systems. Phys. Rev. E **97**(5) (2018)
Krause, A.L., Klika, V., Woolley, T.E., Gaffney, E.A.: From one pattern into another: analysis of Turing patterns in heterogeneous domains via WKBJ. J. R. Soc. Interface **17**(162), 20190621 (2020)
Krause, A.L., Klika, V., Halatek, J., Grant, P.K., Woolley, T.E., Dalchau, N., Gaffney, E.A.: Turing patterning in stratified domains. Bull. Math. Biol. **82**(10), 1–37 (2020)
Krause, A.L., Gaffney, E.A., Maini, P.K., Klika, V.: Modern perspectives on near-equilibrium analysis of turing systems. Philos. Trans. R. Soc. A: Math. Phys. Eng. Sci. **379**(2213), 20200268 (2021)
Kreyszig, E.: Advanced Engineering Mathematics, 8th edn. Wiley-India, UK (2007)
Kuttler, J.R., Sigillito, V.G.: Eigenvalues of the Laplacian in two dimensions. SIAM Rev. **26**(2), 163–193 (1984)
Lamé, G.: Mémoire sur la propagation de la chaleur dans les polyèdres, et principalement dans le prisme triangulaire régulier, volume 22 (1833)
Landge, A.N., Jordan, B.M., Diego, X., Müller, P.: Pattern formation mechanisms of self-organizing reaction-diffusion systems. Dev. Biol. **460**(1), 2–11 (2020)
Leppä, T.: nen. Computational Studies of Pattern Formation in Turing Systems. PhD thesis (2004)

Maass, F., Martin, P.: Precise analytic approximations for the Bessel function $J_1(x)$. Results Phys. **8**, 1234–1238 (2018)
Maini, P.K., Woolley, T.E., Gaffney, E.A., Baker, R.E.: The Once and Future Turing, chapter 15: Biological Pattern Formation. Cambridge University Press (2016)
Maini, P.K., Woolley, T.E.: The Turing Model for Biological Pattern Formation. Springer, pp. 189–204 (2019)
Maini, P.K., Painter, K.J., Chau, H.N.P.: Spatial pattern formation in chemical and biological systems. J. Chem. Soc. Faraday Trans. **93**(20), 3601–3610 (1997)
Maini, P.K., Woolley, T.E., Baker, R.E., Gaffney, E.A., Lee, S.S.: Turing's model for biological pattern formation and the robustness problem. Interface Focus **2**(4), 487–496 (2012)
McCartin, B.J.: Laplacian Eigenstructure of the Equilateral Triangle. Hikari Limited (2011)
McCartin, B.J.: Eigenstructure of the equilateral triangle, Part II: the Neumann problem. Math. Probl. Eng. **8**(6), 517–539 (2002)
McCartin, B.J.: Eigenstructure of the equilateral triangle, Part I: the Dirichlet problem. SIAM Rev. **45**(2), 267–287 (2003)
McCartin, B.J.: Eigenstructure of the equilateral triangle Part III. The Robin problem. Int. J. Math. Math. Sci. **2004**(16), 807–825 (2004)
McCartin, B.J.: On polygonal domains with trigonometric eigenfunctions of the Laplacian under Dirichlet or Neumann boundary conditions. Appl. Math. Sci. **2**(57–60), 2891–2901 (2008)
Morgenthaler, G. W., Reismann, H.: Zeros of first derivatives of Bessel functions of the first kind, $J_n'(x)$, $21 \leq n \leq 51$, $0 \leq x \leq 100$. J. Res. Natl. Bur. Stan. (1963)
Murray, J.D.: Mathematical Biology II: Spatial Models and Biomedical Applications, 3rd edition, vol. 2. Springer (2003)
Nicolis, G.: Introduction to Nonlinear Science. Cambridge University Press, Cambridge (1995)
Olver, P.J.: Introduction to Partial Differential Equations. Springer, Berlin (2014)
Ouyang, Q., Swinney, H.L.: Transition from a uniform state to hexagonal and striped Turing patterns. Nature **352**(6336), 610–612 (1991)
Pinsky, M.A.: The eigenvalues of an equilateral triangle. SIAM J. Math. Anal. **11**(5), 819–827 (1980)
Pinsky, M.A.: Completeness of the eigenfunctions of the equilateral triangle. SIAM J. Math. Anal. **16**(4), 848–851 (1985)
Pockels, F.: Uber die Partielle Differentialgleichung $\Delta u + k_2 u$. BG Teubner (1891)
Práger, M.: Eigenvalues and eigenfunctions of the Laplace operator on an equilateral triangle. App. Math. **43**(4), 311–320 (1998)
Ramm, A.G.: A simple proof of the Fredholm alternative and a characterization of the Fredholm operators. Am. Math. Monthly **108**(9), 855–860 (2001)
Rudovics, B., Dulos, E., De Kepper, P.: Standard and nonstandard Turing patterns and waves in the CIMA reaction. Phys. Scr. **T67**, 43–50 (1996)
Sabatini, L.: Estimation of vibration frequencies of linear elastic membranes. Appl. Math. **63**(1), 37–53 (2018)
Schnakenberg, J.: Simple chemical reaction systems with limit cycle behaviour. J. Theor. Biol. **81**(3), 389–400 (1979)
Schneider, G., Uecker, H.: Nonlinear PDEs, vol. 182. American Mathematical Society (2017)
Scholes, N.S., Schnoerr, D., Isalan, M., Stumpf, M.P.H.: A comprehensive network atlas reveals that turing patterns are common but not robust. Cell Syst. **9**(3), 243–257 (2019)
Schumacher, L.J., Woolley, T.E., Baker, R.E.: Noise-induced temporal dynamics in Turing systems. Phys. Rev. E **87**(4), 042719 (2013)
Sheth, R., Marcon, L., Bastida, M.F., Junco, M., Quintana, L., Dahn, R., Kmita, M., Sharpe, J., Ros, M.A.: Hox genes regulate digit patterning by controlling the wavelength of a Turing-type mechanism. Science **338**(6113), 1476–1480 (2012)
Shortley, G.H., Weller, R.: The numerical solution of Laplace's equation. J. Appl. Phys. **9**(5), 334–348 (1938)
Stanley, H.E.: Introduction to Phase Transitions and Critical Phenomena. Oxford University Press, Oxford (1987)
Tan, Z., Chen, S., Peng, X., Zhang, L., Gao, C.: Polyamide membranes with nanoscale Turing structures for water purification. Science **360**(6388), 518–521 (2018)
Tolstov, G.P.: Fourier Series. Dover Publications (2012)
Turing, A.M.: The chemical basis of morphogenesis. Philos. Trans. R. Soc. Lond. B **237**, 37–72 (1952)

Uecker, H.: Numerical continuation and bifurcation in nonlinear PDEs. SIAM (2021)
Uecker, H., Wetzel, D., Rademacher, J.D.M.: pde2path: a Matlab package for continuation and bifurcation in 2D elliptic systems. Numer. Math.: Theory: Methods Appl. **7**(1), 58–106 (2014)
Vittadello, S.T., Leyshon, T., Schnoerr, D., Stumpf, M.P.H.: Turing pattern design principles and their robustness. Philos. Trans. R. Soc. A: Math. Phys. Eng. Sci. **379**(2213), 20200272 (2021)
Watson, G.N.: The Zeros of Bessel functions. Proc. R. Soc. Lond. A **94**(659), 190–206 (1918)
Weber, E.L., Woolley, T.E., Yeh, C.-Y., Ou, K.-L., Maini, P.K., Chuong, C.-M.: Self-organizing hair peg-like structures from dissociated skin progenitor cells: new insights for human hair follicle organoid engineering and Turing patterning in an asymmetric morphogenetic field. Exp. Dermatol. **28**, 355–366 (2019)
Winter, M., Wei, J., Iron, D.: Stability analysis of turing patterns generated by the Schnakenberg model. J. Math. Biol. **49**, 358–390 (2004)
Wollkind, D.J., Manoranjan, D.J., Zhang, L.: Weakly nonlinear stability analyses of prototype reaction-diffusion model equations. SIAM Rev., pp. 176–214 (1994)
Woolley, T.E., Baker, R.E., Maini, P.K.: The incomputable, chapter turing's theory of morphogenesis: where we started, where we are and where we want to go, pp. 219–235. Springer (2017a)
Woolley, T.E., Baker, R.E., Maini, P.K.: The Turing Guide, Chapter 35: Turing's Theory of Morphogenesis. Oxford Univ Press (2017)
Woolley, T.E.: Spatiotemporal Behaviour of Stochastic and Continuum Models for Biological Signalling on Stationary and Growing Domains. Ph.D. thesis, University of Oxford (2011)
Woolley, T.E.: Pattern production through a chiral chasing mechanism. Phys. Rev. E **96**(3), 032401 (2017)
Woolley, T.E.: Boundary conditions cause different generic bifurcation structures in Turing systems. Bull. Math. Biol. **84**(9), 1–38 (2022)
Woolley, T.E., Baker, R.E., Maini, P.K., Aragón, J.L., Barrio, R.A.: Analysis of stationary droplets in a generic Turing reaction-diffusion system. Phys. Rev. E **82**(5), 051929 (2010)
Woolley, T.E., Baker, R.E., Gaffney, E.A., Maini, P.K.: Power spectra methods for a stochastic description of diffusion on deterministically growing domains. Phys. Rev. E **84**(2), 021915 (2011)
Woolley, T.E., Baker, R.E., Gaffney, E.A., Maini, P.K.: Influence of stochastic domain growth on pattern nucleation for diffusive systems with internal noise. Phys. Rev. E **84**(4), 041905 (2011)
Woolley, T.E., Baker, R.E., Gaffney, E.A., Maini, P.K.: Stochastic reaction and diffusion on growing domains: understanding the breakdown of robust pattern formation. Phys. Rev. E **84**(4), 046216 (2011)
Woolley, T.E., Baker, R.E., Gaffney, E.A., Maini, P.K., Seirin-Lee, S.: Effects of intrinsic stochasticity on delayed reaction-diffusion patterning systems. Phys. Rev. E **85**(5), 051914 (2012)
Woolley, T.E., Baker, R.E., Tickle, C., Maini, P.K., Towers, M.: Mathematical modelling of digit specification by a sonic hedgehog gradient. Dev. Dyn. **243**(2), 290–298 (2014)
Woolley, T.E., Maini, P.K., Gaffney, E.A.: Is pigment cell pattern formation in zebrafish a game of cops and robbers? Pig. Cell Melan. Res. **27**(5), 686–687 (2014)
Woolley, T.E., Krause, A.L., Gaffney, E.A.: Bespoke turing systems. Bull. Math. Biol. **83**(5), 1–32 (2021)